Dynamic Retrieval of Olive Tree Properties Using Bayesian Model and Sentinel-2 Images

Hana Abdelmoula [ID], Abdelaziz Kallel [ID], Jean-Louis Roujean [ID], and Jean-Philippe Gastellu-Etchegorry [ID]

Abstract—The goal of this study is to provide a fine detection and monitoring of olive orchard trees over large areas to antici-pate any damage. We developed an original method to assess the spatiotemporal dynamics of biophysical parameters in the olive orchards using satellite observations and radiative transfer models. Sentinel-2 time-series data collected over a four-year period were fused with Planet images from the same time period to enhance the temporal trends in olive orchards in the Sfax region located in southern Tunisia. These images also served to extract soil spec-trum variations required by the 3-D discrete anisotropic radiative transfer model to account for canopy background effect. As a backward model, we developed an original technique based on the Markov chain Monte Carlo method that has the advantage of being able to model sensor noise and account for spatial and temporal regularization. It allows retrieving key parameters such as leaf area index (LAI), chlorophyll content, water content, and mesophyll structure. Taking advantage of 1) the Sentinel-2 images downscaled to a moderate resolution of 80 m to ensure representative pixels of the local mixing (i.e., trees and soil); 2) the appropriate soil signature derived from high spatial and spectral resolution image; and 3) the accuracy of the direct and inverse modeling, it was possible to retrieve the plant properties even when LAI values are less than 0.14. Indeed, our inversion results show that the estimated parameters are strongly correlated especially with the LAI field measurements with $R^2 = 0.9937$.

Index Terms—Biophysical properties, discrete anisotropic radiative transfer (DART), Markov chain Monte Carlo (MCMC), olive trees, planet, Sentinel-2, time series.

I. INTRODUCTION

ESTIMATING the biophysical properties of olive tree or-chards is mandatory as it has a tremendous impact on the agricultural field management, the vegetative decay, and also for farmers, leading to monitoring health and estimating yield. Leaf area index (LAI), chlorophyll content (Cab), and other leaf biochemical components, such as dry matter (Cm), water content (Cw), and mesophyll structure (N) are indeed the meaningful parameters to better characterize olive crops in their growing stage [1]. Any anomaly in the derivation of such biophysical parameters is useful piece of information to detect stress or disease [2]. These anomalies could be seen using Sentinel-2 satellite data, mostly because of the red-edge (RE) spectral regions sensitive to photosynthetic pigment absorption. In addition, the short revisit interval at moderate latitudes of this satellite offers important temporal information on short-term changes in vegetation across broad regions. Recent research using Sentinel-2 data revealed the sensor's ability to monitor biophysical parameters such as chlorophyll content [3] and LAI [4], [5]. Therefore, Sentinel-2 data are deemed relevant for vegetation monitoring, especially for heterogeneous and complex canopies [6].

Sentinel-2 has a spatial resolution, which leads to mixed pixels in our study area such like it is difficult to disentangle the soil and vegetation components, whereas it is mandatory to support our modeling approach. This is crucial since the canopy is seldom closed in the case of olive orchards [7]. In addition, as a result of agriculture practices and vegetation phenology in these landscapes, soil varies spatially and seasonally. It is worth recalling that Planet scenes have a 3-m spatial resolution but limited spectral information. Moreover, they do not cover the RE nor shortwave infrared domain. At least, this satellite presents the asset of being able to acquire daily global images with small swath width. When combined with other satellite data, it offers the ability to monitor vegetation at regional scale [8], [9] like monitoring tropical forest carbon stocks and emissions [10]. As a result, merging Planet with Sentinel-2 images provides a high spatial well-defined spectral product allowing the extraction of soil spectrum variations to properly account for the influence of the soil background.

Most approaches link the vegetation monitoring with the retrieval of biophysical variables from satellite observations, including the use of empirical and radiative transfer models (RTMs) [11]–[13]. These latter have proven their strong poten-tial for estimating biophysical parameters. RTMs can solve some of the drawbacks of purely empirical techniques by reducing reliance on field measurements and modeling the reflectance mixture formed by the contribution of various components at medium resolutions (e.g., 80 m). These two elements are critical for enhancing the retrieval of biophysical parameters over time. While some popular 1-D RTMs for uniform canopies, like the scattering by arbitrarily inclined leaves (SAIL) model, provide computationally efficient solutions, they are severely limited in their ability to depict quite heterogeneous and discontinuous

canopies [14]. Such category of models requires handling complex 3-D RTMs that account for realistic tree canopy structure and soil effects. Previous research have used the 3-D forest light interaction model to represent tree canopies in a 3-D manner and to conduct spatial and spectral scaling of several biophysical parameters [15], [16]. Moreover, to the best of our knowledge, none of these models account for the impact of soil on spectral reflectance in open canopies and dealt with biophysical properties for a monitoring at high spatial and temporal resolution in open canopies like olive orchards. In such natural environments, soil variations are extremely relevant and have a large influence on time-series data processing over versatile sparse canopies [17]. Other RTMs, such as the discrete anisotropic radiative transfer (DART) model [18], [19], have addressed these constraints and are found especially useful for canopy modeling. The RTM inversion techniques to retrieve the biophysical parameters from Sentinel-2 simulated data and also the investigation of the inversion methods have been outlined in [14] and [20]. The lookup table (LUT), the quasi-Newton (QNT) [21], and the neural network (NNT) [22] are the most popular techniques used to solve the inverse problem. The LUT method has been widely used to invert the RTM for the estimation of canopies biophysical parameters [23] since it is simple to implement and is low demanding in terms of computation time compared to other methods. Indeed, it seeks the closest simulated observation to the real measurement from a database of simulated observations, rather than requiring *a priori* information as in the QNT approach. Furthermore, unlike the NNT, it does not require a huge training database. However, there are some limitations inherent to the LUT method, such as it cannot model the *a priori* information about the parameter distributions. Moreover, the LUT method cannot predict errors caused by observation noise and reflectance model inaccuracy, which degrades the performance of the retrieval. On the other hand, the inverse problem do not have a unique solution due to the presence of uncertainties in the datasets and also the possible inadequacy of RTM simulations. To overcome such issues, applying Bayesian models to RTM inversion processes provides a straightforward way to quantify the covariance and uncertainty of parameter estimates while integrating different sources of information. RTM inversion has relied on the use of independent prior information to address the otherwise underdetermined challenge of estimating a high number of parameters from a limited number of observations [21], [24], [25]. As these studies neglect the parameter uncertainties or just approximate it, recent research has showed the efficiency of the hierarchical Bayesian technique called the Markov chain Monte Carlo (MCMC) methods [26], [27]. Nevertheless, to the best of our knowledge, such methods have yet to be applied for satellite time-series data. In this case, it will be useful to add regularization techniques with the spatial criterion to prevent from outliers and the temporal criterion to reduce time-series fluctuation mainly due to atmospheric conditions. The objective of this article is to estimate the biophysical variables (LAI, Cab, Cw, and N) of olive tree orchards based on fused Sentinel-2 and Planet images covering a period of four years. An original forward/backward modeling approach is presented herein based on the combined use of a 3-D RTM DART and an MCMC
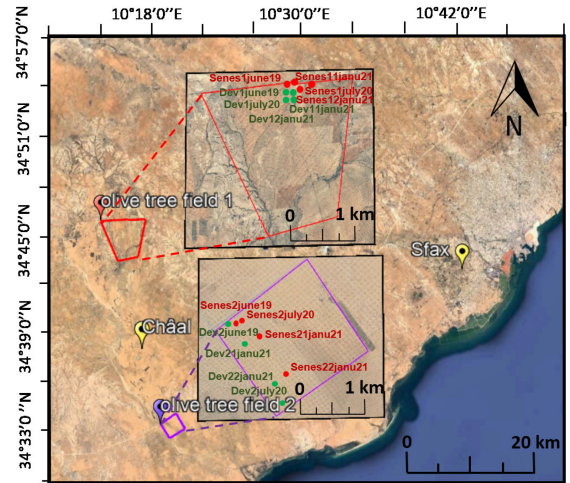

Fig. 1. Location of the study areas in Châal, Sfax, Tunisia from Google maps.

TABLE I
FIELD MEASUREMENT ACQUISITION DATES AND MEASURED GROUP LABELS

Acquisition date and field		Measured groups labels	
		Well-developed trees	Senescent trees
June 21th,2019	Field1	Dev1june19	Senes1june19
	Field2	Dev2june19	Senes2june19
July 31th,2020	Field1	Dev1july20	Senes1july20
	Field2	Dev2july20	Senes2july20
January 31th,2021	Field1	Dev11janu21	Senes11janu21
		Dev12janu21	Senes12janu21
	Field2	Dev21janu21	Senes21janu21
		Dev22janu21	Senes22janu21

approach including a spatial and temporal regularization. This method is evaluated using satellite data collected at two different sites and is further validated using ground-based measurements.

II. MATERIALS

A. Data Collection

1) Study Area: The study site is located in Châal (Sfax, southern Tunisia) ($34°37'27.77''$N, $10°17'33.78''$E) and consisted of a 17 500-ha commercial olive area. The main olive cultivar is Chemlali grown in southern Tunisia. Within this area, two olive orchards, field 1 and field 2, with an area of 1704 and 419 ha, respectively, were selected as they differ in soil and olive tree properties (see Fig. 1). The soil of field 1 is a marginal soil (clay and gypsum), whereas the soil of field 2 is a deep sandy soil. Note that distance between two successive olive trees is always 24 m. The Sentinel-2 pixel resampled to 80-m resolution covers an area that contains around 11 olive trees. Hence, each measured group contains four homogeneous trees, either well developed or senescent, rather than a unique tree. Table I displays the field measurement acquisition dates and the measured group labels. Table II displays the variability of the set of collected biophysical parameters and olive tree dimension for each group. Field 2 olive trees are more developed than those of field 1.

TABLE II
LAI, CAB, CW, AND TREE DIMENSION (HEIGHT × WIDTH) GROUND MEASUREMENTS

| Group	$LAI(m^2|m^2)$			$Cab(\mu g|cm^2)$			$Cw(g|cm^2)$			Tree dimension(m)		
	Min	Max	Mean	Min	Max	Mean	Min	Max	Mean	Min	Max	Mean
Dev1june19	0.1011	0.13	0.1208	14.2383	67.5976	54.1833	0.0193	0.02	0.0198	4×6	6×8	5×7
Senes1june19	0.02	0.05	0.0392	20.3951	71.0181	55.95	0.0134	0.0155	0.0151	3×3	4.5×4	3.5×3.5
Dev1july20	0.1054	0.1512	0.1343	61.63	65.40	54.66	0.0156	0.0177	0.0169	3.5×4.5	5×6.5	5× 5
Senes1july20	0.0021	0.0261	0.0129	10.1344	38.5721	28.3387	0.0126	0.0132	0.0122	2×3	3.5×3.5	3.5×3.5
Dev11janu21	0.1022	0.1435	0.1108	31.63	75.40	63.20	0.0188	0.02	0.01926	3.5×4.5	5.5×7	5×6.5
Senes11janu21	0.0091	0.0208	0.0119	20.15	68.861	56.3257	0.0009	0.0019	0.001	2.5×3	3.5×3.5	3.5×3
Dev12janu21	0.0258	0.0516	0.0452	21.14	75.2	55.558	0.0176	0.0192	0.0189	4.5×4	5.5×6.5	5×5.5
Senes12janu21	0.0095	0.0251	0.0186	10.153	68.47	52.93	0.0096	0.0112	0.0108	2.5×3.5	3.5×4	3.5×3.5
Dev2june19	0.107	0.14	0.1212	16.1485	52.1626	49.5427	0.011	0.019	0.0172	5×6	7×8.5	5.5×7.5
Senes2june19	0.008	0.039	0.0174	17.6587	79.2272	50.8867	0.013	0.0155	0.0148	3×2.5	4×3.5	3×3
Dev2july20	0.0792	0.0816	0.0804	51.9535	59.3874	55.585	0.0155	0.0161	0.0154	3.5×4	5×6	4.5×4
Senes2july20	0.008	0.039	0.01	50	40.7270	24.6966	0.0102	0.0124	0.011	2×2	3×3.5	3×3
Dev21janu21	0.1012	0.1256	0.1144	34.926	69.345	48.7369	0.0155	0.0183	0.0179	4×4	5.5×7	5×4.5
Senes21janu21	0.0089	0.024	0.0115	10.148	48.28	39.75	0.0104	0.0128	0.0119	2.5×2	3.5×3	3×3
Dev22janu21	0.0095	0.1286	0.1103	33.356	69.127	57.8636	0.0165	0.0191	0.0184	3.5×4	6×6.5	5×4.5
Senes22janu21	0.0094	0.029	0.0154	10.478	30.953	22.66	0.0101	0.0133	0.012	2×3	3.5×3.5	4×3
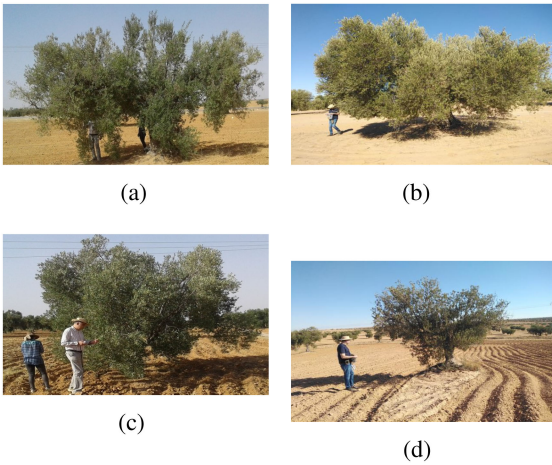
Fig. 2. Field 1 olive tree sample images of the measured groups. (a) Tree from Dev1june19. (b) Tree from Dev1july20. (c) Tree from Senes1june19. (d) Tree from Senes1july20.

Note that none of the two sites were irrigated. The local climate of the area is classified Mediterranean, which is characterized by hot and dry summers and cool winters plus the scarcity of rainfall events, estimated to 282 mm per year in average, occurring mostly during the fall and autumn-winter-time seasons (September–March).

2) LAI Acquisition: Over each field, a mean estimate of the biophysical parameters was achieved from the four trees of each group. The LAI was measured by calculating the gap fraction using olive tree images taken by a smartphone. The latter was positioned under each olive tree crown at 0.5-m distance from the ground in eight different positions. With the clumping effect caused by the 3-D architecture of the tree, the resulting image as shown in Fig. 2 included both leafy and woody materials. The LAI ground-truth derivation protocol from smartphone images will be detailed in Section IV-D.

3) Cw and Cab Measurement Protocol: For the Cw measurements, ten individual leaves (with around 70% exposed to the sun) were randomly collected from the top layer of each tree.

To improve the accuracy, three repetitive measurements were achieved for each group of trees, and then, the mean value of the four trees was finally calculated. Before each measurement of Cw, the sampled leaf is weighed and then dried in an oven at 65° during 48 h to measure the weight of the dry leaf. Cw is calculated by [28]

$$\text{Cw} = \frac{\text{FW} - \text{DW}}{S} \quad (\text{g/cm}^2) \qquad (1)$$

where FW is the weight of the fresh leaf (g), DW is the weight of the completely dried leaf (g), and S is the surface area of the leaf (expressed in cm^2) that is measured with an ADC AM-350 leaf area meter.

The Konica Minolta SPAD-502 leaf chlorophyll meter, which is a hand-held device, was used for the measurement of Cab. For each tree, we measured 20 individual leaves randomly selected with about 70% exposed to the sun, and we calculated the mean value. To measure Cab accurately, a calibration relationship is required between the chlorophyll meter readings and Cab content measured in the laboratory according to a suggested procedure [29]. We used the calibration relationship proposed by [30] for olive trees in nonirrigated fields

$$\text{Cab} = 0.8271 \times \text{SPAD} - 12.8; (R^2 = 0.84). \qquad (2)$$

Equation (2) converts the SPAD readings into leaf Cab contents.

4) Satellite Data Acquisition: In order to test our algorithm, Planet and Sentinel-2 data time series during four consecutive years from January 2017 to January 2021 over Châal region were processed and analyzed. Sentinel-2 images were fused with Planet images to reach a 3-m resolution. The Planet image acquisition date was as close as possible in time to the Sentinel-2 image acquisition, on the same day or at worst day before or after. Due to frequent high cloud coverage throughout the rainy season in the study areas, our time series include only one image per month, which appears to be sufficient for monitoring olive trees. The Sentinel-2 multispectral imager instrument (MSI) Level 2-A image covering Sfax (particularly Châal) is an atmospheric corrected product issued from the French Land Data Center (THEIA: theia.cnes.fr). The product is radiometrically calibrated into bottom-of-atmosphere (BOA) reflectance data. The

TABLE III
CORRESPONDING LAI VALUES TO THE LEAF NUMBER

Leaf number	LAI
58000	0.0092
158000	0.0155
258000	0.0465
358000	0.1023
458000	0.1312
558000	0.2057
658000	0.2881

Planet images are distributed as a four-band product (P1 = blue, P2 = green, P3 = red, and P4 = near infrared) and downloaded as a Planet Surface Reflectance image product. These images are atmospherically corrected to BOA reflectance.[1] Sentinel-2 provides spectral data in 13 bands from 443 to 2200 nm [14]. A selection of Sentinel-2 10- and 20-m pixel resolution bands (S2, S3, S4, S5, S6, S7, S8, S8a, and S11) covering VIS, RE, NIR, and SWIR spectral ranges were considered to retrieve the vegetation properties as they are recommended to capture vegetation features [25].

III. PHYSICAL BASEMENT

A. Forward Radiative Transfer Modeling

To create as realistic simulations as possible, an accurate forward RTM is required. The latter entails creating a LUT database with free parameters and simulated reflectance spectra. These RTMs take as input the biophysical parameters and the scene architecture and geometry to simulate reflectance. Inversion of these models provides an estimate of biophysical parameters given reflectance values as input. In this study, two RTMs were coupled to estimate the biophysical parameters of the vegetation: the DART model at canopy level was linked with the PROperties SPECTra (PROSPECT) leaf model, thereby combining canopy and leaf attributes. The DART model is able to simulate the radiation propagation in complex 3-D scenes for the entire optical domain from mock-ups created with 3-D imported objects composed of a set of triangle groups. The elements of each group have the same optical properties (i.e., same scattering function). To cover various scenarios of LAI, several mock-ups can be created with different leaf density. Moreover, DART simulations take into account the atmospheric conditions of illumination and the geometry of the scene, that is the direction of the sensor and the sun, which results in a realistic simulation of a satellite image.

The PROSPECT model [31] calculates leaf hemispherical reflectance and transmittance as a function of Cab, Cw, and N in addition to the leaf dry matter content Cm and the leaf carotenoid content Car. The coupled model is deemed enough accurate as it provides realistic satellite observations [18]. In our case, the model simulations allow us to link the Sentinel-2 reflectance to the olive tree properties. The parameterization of the DART and PROSPECT models is detailed in Section IV-B1 and Table IV.

IV. METHODOLOGY

The approach followed to retrieve olive tree biophysical properties relies on an inversion method applied to time series of

[1][Online]. Available: https://assets.planet.com/marketing/PDF/Planet-Surface-Reflectance-Technical-White-Paper.pdf/

Smartphone image

Fig. 3. Smartphone image from group Dev1june19.

satellite image. The different steps of the developed approach are summarized in Fig. 3. The algorithm inputs are the Sentinel-2 and Planet image time series (step 1), and the outputs are the maps of the inverted biophysical properties. These latter are generated at a degraded spatial resolution (i.e., 80 m). Indeed, a medium-resolution map is all needed because the Châal region is wide with 17 500 ha of olive tree crops, and getting information at a very high resolution is difficult to exploit because it could be only bare soil. The basic pattern must even be larger to integrate all landscape components. Therefore, the retrieval procedure applies to downsampled Sentinel-2 images. Some preprocessing was applied on the Sentinel-2 and Planet images to estimate the soil background reflectance (step 2). Considering that a Sentinel-2 image contains mixed pixels, the different components of the reflectance are evidenced from the sharpened Sentinel-2 image at the Planet resolution using the TsHARP method (see Section IV-A2). Particularly, the fused Sentinel-2 and Planet images were split into olive tree and surface units. Besides, a ground classification was performed to distinguish the various soils that affect differently the spectral signature of the satellite pixels. The LUT generation was performed by simulating many Sentinel-2 observations of olive tree fields for a set of predefined biophysical parameters: LAI, N, Cab, and Cw as well as soil reflectance (step 3). The resulting simulated database serves as input for the LUT inversion (used as a comparison method), which consists of retrieving the optimal set of biophysical properties in the LUT database from the best similarity criterion with the actual observation. The LUT database is also found useful for the developed methods: MCMC for single date inversion and MCMCtimeseries for multidate inversion. These latter allow us to take into account statistical constraints such as the spatiotemporal regularization. Finally, the MCMC inversion approach is performed as well as the MCMCtimeseries inversion approach (step 4). For the LAI measurement protocol, smartphone images are used to calculate the gap fraction that serves to derive LAI olive tree ground value. In the following, these steps are described in separate sections.

A. Preprocessing Steps

1) Downsampling: The DART model serves to simulate olive tree images as realistically as possible. An image composed of a single olive tree and its surrounding soil background is then generated. Such an image is assumed to contain a sufficient degree of heterogeneity to be representative of the landscape

TABLE IV
INPUT PARAMETERS USED FOR CREATING THE LUT

Symbol	Value	Units
Leaf parameters (PROSPECT-4)		
$\theta_1 = N$	1:0.5:3	-
$\theta_2 = Cab$	20:10:90	$\mu g\|cm^2$
$\theta_3 = Cw$	{0.002; 0.0053; 0.012; 0.025; 0.05}	$g\|cm^2$ or cm
$\theta_{c1} = Cm$ [a]	{0.003; 0.013; 0.023; 0.033; 0.043}	$g\|cm^2$
$\theta_{c2} = Car$ [b]	5:5:25	$\mu g\|cm^2$
Canopy parameters (DART)		
$\theta_4 = LAI$	{0.0092;0.0155;0.0465;0.1023;0.1312;0.2057;0.2881}	-
$\theta_5 = \rho_s$	1:1:10	-
$\theta_6 = $ Tree height	3-6	m
$\theta_7 = $ Crown diameter	3-8	m
$\theta_8 = $ Solar zenith angle	0-90	Degrees
$\theta_9 = $ Solar azimuth angle	0-180	Degrees
$\theta_{10} = $ Viewing zenith angle	0-90	Degrees
$\theta_{11} = $ Viewing azimuth angle	0-180	Degrees

[3a] The value for generating the LUT was held constant at its mean value (0.02).

[3b] The value for generating the LUT was held constant at its mean value (15).

[3] The variation interval of the parameters θ_1, θ_2, θ_{c2}, and θ_5 is presented by minimal value:step:maximal value. The soil values correspond to the class number, as explained in Section IV-A3.

variability. In the case of dense vegetation, the soil effect is not so much important, and the canopy reflectance solely would be needed to ensure an accurate retrieval of the vegetation properties. However, in the present case, as the distance separating two olive trees is 24 m, the soil effect plays an important role and must be included in the retrieval procedure to avoid an erroneous estimate of the biophysical properties. Sentinel-2 images of 10- and 20 m pixel resolutions are composed of mixed pixels varying from pure soil to dense vegetation. In the inversion process, the mixed pixels contain too unknown information to be compared to DART averaged reflectance. At 10 m, pixels could be pure soil or tree crown. At 20 m, the pixel cannot either represent a sequence of the scene since the distance between two trees is 24 m. Therefore, a degraded image is needed to better represent the local heterogeneity of the field. At 40 and 60 m, we noticed that pixels are varying due to their compositions: for instance, high brightness mainly in the visible domain if the number of trees is low. At 80 m, this dependence vanishes and is hidden in the pixels signature. For this reason, images are downsampled to this resolution, which is deemed, somewhat arbitrary, as the best tradeoff between minimizing the heterogeneity and maximizing the resolution.

2) Fusion/Correction: Hitherto, Sentinel-2 satellite imagery is broadly exploited for vegetation detection and monitoring in huge areas. Information on the soil background reflectance can constrain the solution space and, therefore, enhance the inversion accuracy, overall the precision on retrieved vegetation parameters. This is especially the case when the soil is very bright and may be largely influent. In this case, the total reflectance is highly influenced by the soil properties. To disentangle soil and vegetation components, we propose to fuse Sentinel-2 with Planet images that propose a very high spatial resolution. The two satellites Planet and Sentinel-2 do not share exactly the same spectral bands. To overcome this problem, the fusion approach is achieved in two steps using the response functions. The first one, using the TsHARP method [32] applied to the Sentinel-2 image of 10-m resolution, we obtain a sharpened product at 3-m resolution using the Planet image at this same resolution by

tuning the average and the standard deviation of the latter to fit the Sentinel-2 image. The second step enhances the sharpened image by correcting the bias produced at 80-m resolution. The result mimics the Sentinel-2 image at 3 m, which further serves to obtain a soil reflectance image at 80-m resolution. This step of the processing drives the pixel reflectance due to brightness.

More precisely, in the first step, Sentinel-2 bands closest to Planet bands are spectrally projected into them. It results that 10 m Sentinel-2 bands 2, 3, 4, and 8 are corrected by the Planet bands 1, 2, 3, and 4, respectively. Besides, 20 m Sentinel-2 bands 5, 6, 7, 8A, and 11 are corrected by the Planet band 4. The fusion is achieved by modifying the mean and the standard deviation of the Planet band (P_i) to fit those with the corresponding Sentinel-2 band (S_j), and the new band S_j^3 is given by

$$S_j^3 = \frac{(P_i - m_{P_i})}{\sigma_{P_i}} \times \sigma_{S_j} + m_{S_j} \qquad (3)$$

where m_{S_j} and m_{P_i} are the average of S_j and P_i images, respectively, and σ_{S_j} and σ_{P_i} are the corresponding standard deviation.

Correcting S_j^3 reduces the distortion effect between Planet and Sentinel-2 spectral bands. It is worth remembering that, in the ideal case, downsampled S_j^3 to the resolution of S_j should be equal to S_j, which is not precisely the case after the first step. Therefore, in the second step, we propose to correct the local average of S_j^3 by S_j. However, due to the misregistration issues between P and S, such a processing could generate additional artifacts at 10-m resolution. To overcome this problem, we propose to correct S^3 average by S downsampled to 80 m (S^{80}). In this case, for each S^{80} pixel (x^{80}), the corresponding pixels at 3-m resolution $(\{x_n^3 / x_n^3 \subset x^{80}, n = 1, \ldots, N\})$ have an averaged value $S^{80}(x^{80})$. Finally, the update of the reflectance of a pixel x_n^3 of each band j of $S^{(3)}$ is given by

$$S_j^{(3)}(x_n^3) \leftarrow S_j^{(3)}(x_n^3) - m_{S_j}^3 \{x_n^3\}_{n=1,\ldots,N} + S_j^{80}(x^{80}), \quad (4)$$

where $m_{S_j}^3 \{x_n^3\}_{n=1,\ldots,N}$ is the average of S_3 over $\{x_n^3\}_{n=1,\ldots,N}$.

3) Trees and Ground Detection: In this section, we proceed to the detection of olive trees and to the derivation of the intensity
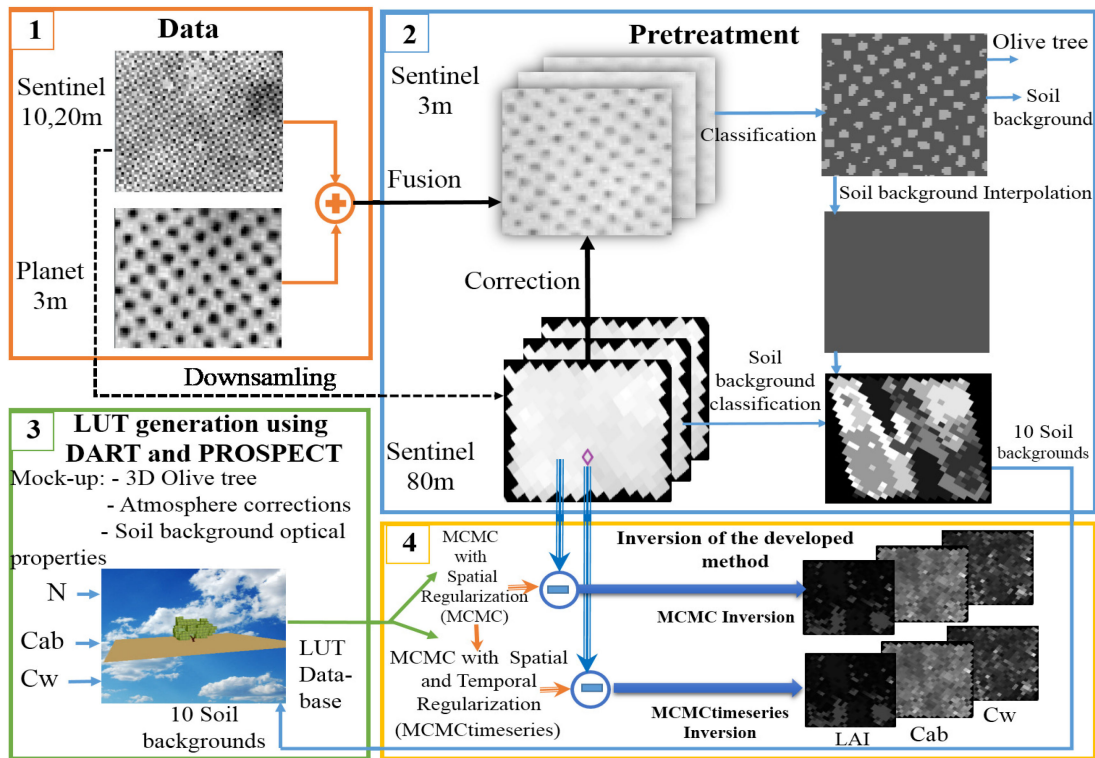
Fig. 4.   Schematic diagram of the different steps of the olive tree biophysical property retrieval.

of soil reflectance surrounding each tree. To build realistic mock-ups, background reflectance is important as well as tree detection since the distance between two trees and their size form important inputs. Such information can be derived from the product Sentinel-2 at 3-m resolution based on a classification that allows separating ground from trees. Nevertheless, in order to accurately estimate the soil reflectance, it is important to apply a postprocessing that ensures the removal of the mixed pixels from the soil class. Moreover, in order to define the soil over the whole study area, reflectance of pixels that do not belong to this class should be replaced by an expected value of soil reflectance. First, we classified the image between ground and olive trees classes using the Gaussian mixture model (GMM) described in [33], which allows estimating the size and the number of trees (see Fig. 3). Since the simulation of RTM requires a good knowledge of the soil reflectance, it is crucial to obtain a local determination because of its high variability within a landscape scene. For such, we created a soil image delineating the soil reflectance in and around each tree. To do so, the spectral signature of the pixels of the Sentinel-2 and Planet fused images at 3-m resolution belonging to the olive tree class are replaced by the soil signature according to an interpolation scheme (i.e., Bicubic) [34]. Moreover, to ensure the removal of the mixed pixels within the soil class, the olive class is enlarged using the morphological opening tool. It is important to notice that the soil reflectance may vary significantly between the 80-m pixels. Therefore, it is required that mock-ups are ideally generated on a pixel-by-pixel basis. However, this is heavy to implement, and instead, we consider for each date ten classes

for soil. Mock-ups are then created for each class. For pixels having intermediate soil reflectance between classes, the total reflectance is interpolated.

B. DART Simulations

1) LUT Generator: The DART model is used to generate the LUT database to be compared with Sentinel-2 images. Simulations are performed for multispectral Sentinel-2 channels. In the present case, a realistic 3-D mock-up will draw an olive tree every 24 m, which is the constant row distance between two stands. We have retained the mock-up[2] of Fig. 4(a) because it well depicts an olive tree of the Châal region at the peak season. In order to view and modify the chosen 3-D model, we use the Blender[3] 3-D software that permits to adjust the olive tree size (tree height and crown diameter) in removing leafy material. This allows us to produce olive tree mock-ups similarly to the actual ones as well as to get correct LAI values within its physical domain of variations. The seven created olive tree mock-ups are illustrated in Fig. 5. DART simulates our scene using these mock-ups. DART decomposes the optical properties in two groups: one for the leaves and one for the woody material, merely trunk and branches. The optical properties of woody elements are simulated using the predefined spectral response of a bark-spruce-stem of the DART database. The leaf spectral response is simulated using the PROSPECT model.

---

[2]Download   site: https://cgtricks.com/olive-trees-mereces-arch-viz-3d-visualization-studio/
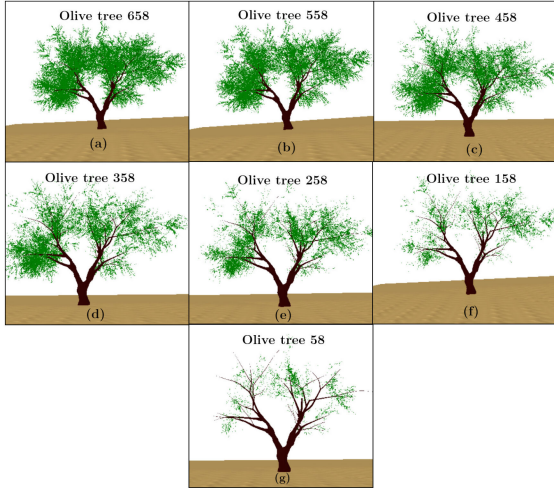
[3]Blender: https://www.blender.org/

Fig. 5. Seven 3-D olive trees used to build the mock-ups: the number presented in the top of each mock-up represents the number of thousands of leaves within the tree.

The LUT is then generated by simulating many observations (14000 simulations) in varying the structural and biophysical properties of interest of the olive tree such as the number of leaves in the tree (proportional to LAI), Cw, Cab, mesophyll structure (N), and soil reflectance (ρ_s).

A sensitivity analysis similar to [35] was conducted to evaluate the impact of each parameter (LAI, Cab, Cw, N, Cm, and Car) on Sentinel-2-simulated canopy reflectance. For such, we modified one DART parameter at the time by specific increments while holding the remaining parameters at their mean values. This served to fix a number of model parameters when generating the LUTs.

Fig. 6 displays the outcomes of DART/PROSPECT sensitivity study to estimate LAI, Cab, Cw, N, Cm, and Car. The simulated canopy signatures are more–less affected by the parameters, as it could be expected. The variable LAI exerts a strong influence on the simulated reflectance of the canopy for all Sentinel-2 channels, particularly on the VIS and NIR spectral bands. This proves that LAI values ranging from 0.0092 to 0.1350 (measured values) can be estimated provided that the soil signature is well known. Variations in Cab primarily changed the reflectance in the visible and RE range (550–750 nm), affecting both the green peak and the RE signatures. N also influenced mainly the visible channels, but its domain of influence covers the whole spectral range, thereby enhancing the level of reflectance simulation. Car produces little variations and only in the vicinity of 530 nm. Cw and Cm barely contribute to variations in the visible. Cw intensely affects the NIR, and mostly, the SWIR and Cm infers small variations in the NIR domain. Finally, it was decided to take fixed values for Car = 15 μg $\cdot$ cm^{-2} and Cm = 0.025 g $\cdot$ cm^{-2} in the LUT generation. The next step consists of optimizing the retrieval of freely variable biophysical parameters.

Seven olive trees are created using the Blender software in varying the number of leaves. Table III illustrates the corresponding LAI value calculated by DART according to the number of leaves to match with the field measurements. The acronyms and the imposed range of the 12 input parameters of DART for LUT creation are indicated in Table IV. The illumination and viewing angles are input parameters of each image. Note that for the variable parameters (i.e., LAI, Cab, Cw, N, Car, Cm, and ρ_s), their values were varied based on the range obtained from the field measurements and from other studies focused on the same crop [36]–[38].

C. Inversion Procedure

1) LUT Database: The inversion procedure using the built LUT database is performed in two steps. The first one consists of generating the LUT inherent to the Sentinel-2 image using the DART model in sampling the solutions space of the retrieved parameters. The second one is activated when a Sentinel-2 image is available. It consists of searching in the precomputed solutions space the one that fits the best image pixel reflectance. Such an inversion procedure is based on computing a cost function that minimizes the differences between measured and simulated reflectance [39]. In the LUT approach, the mean values of n best parameter combinations give the solution [40], [41]. In our case, the root-mean-square error (RMSE) between the measured and simulated reflectance is selected as the cost function.

2) MCMC Method: The inversion is carried on by searching the closest simulation to the actual observation using the LUT technique. However, this technique presents some uncertainty in case of noisy datasets. For such, we improved the inversion technique by taking into account atmospheric effects and sensor noise, also by considering the error on the simulation due to the possible inappropriateness of the forward model. As a result, we choose to use a hierarchical Bayesian modeling to compute the *a posteriori* probability of the different unknown variables and to formulate the *a priori* knowledge. The *a posteriori* probability is not so easy to sample. The Bayesian statistical approach called MCMC is an iterative processing of sampling with, for instance, the Gibbs sampler. At each step of the procedure, only one parameter is sampled according to its conditional probability, while other parameters are fixed. MCMC sampling converges to the *a posteriori* distribution. In this section, we present our developed MCMC approach incorporating the spatiotemporal regularization technique including information from neighboring pixels [42] and from Sentinel-2 image time series [43]. In the following, we present our statistical assumption and then the derivation of the *a posteriori* probability for both spatial and temporal regularization conditions.

Spatial regularization condition: We postulate that any observation R, i.e., the reflectance value for any Sentinel-2 band downsampled pixel, depends on several parameters plus a noise term

$$R = f(\theta) + \varepsilon \qquad (5)$$

where f is a conceptual function that assigns a value from the DART model, $\Theta = (\theta^{(1)}, \theta^{(2)}, \theta^{(3)}, \theta^{(4)})$ is the set of the unknown parameters [$\theta^{(5)}$ corresponding to the soil pixel reflectance, it is not taken into account as it is already precalculated for each pixel using the soil classification], and ε models the cumulative error due to uncertainty assessment in mock-up design
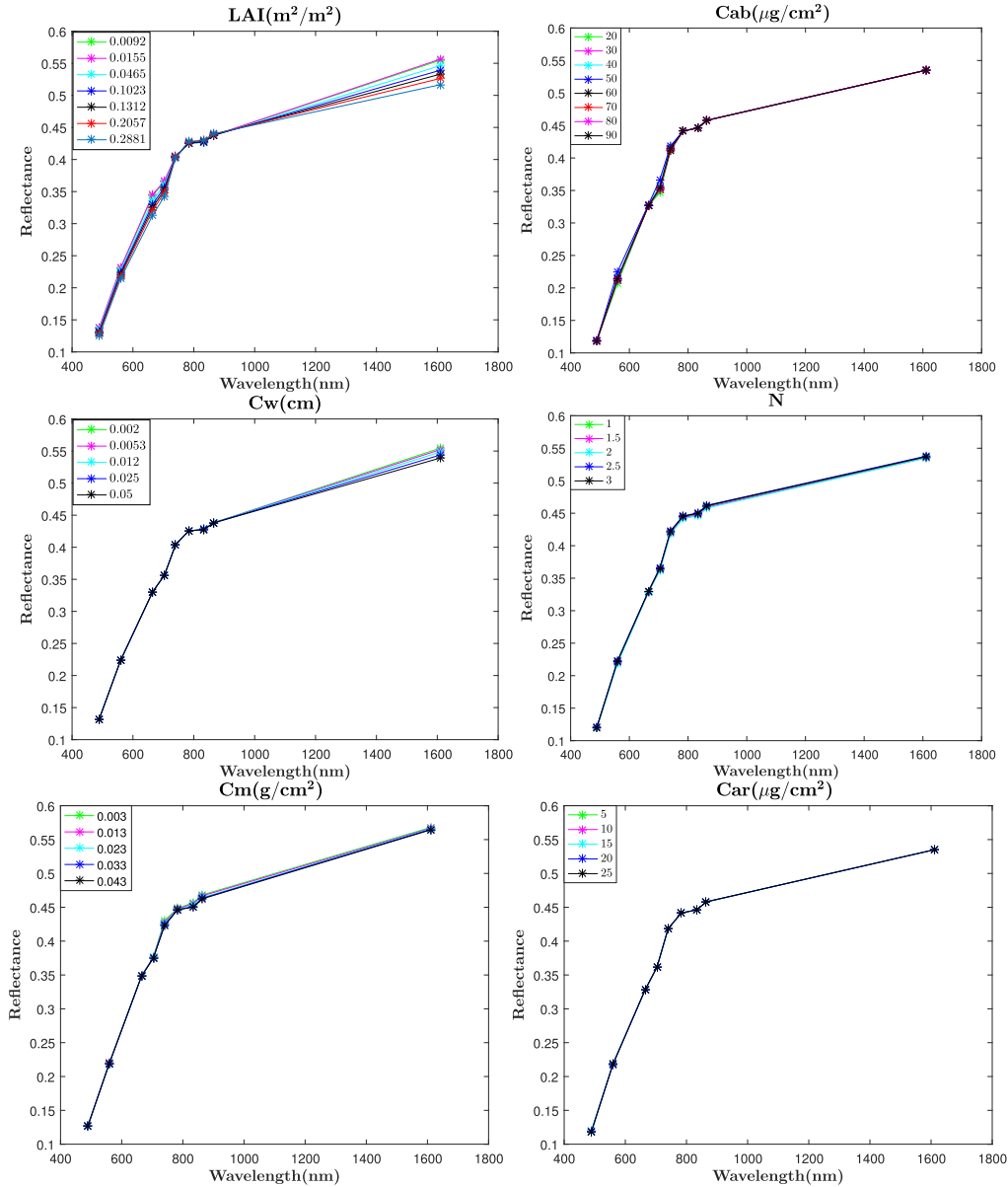
Fig. 6. Variation in the spectral response of the simulated canopy reflectance of Sentinel-2 after varying each DART/PROSPECT parameter (olive tree in 24×24 scene dimension) and keeping all other parameters fixed at their reference values (LAI $= 0.1023$, Cab $= 30\mu g \cdot cm^2$, Cw $= 0.05$ cm, N $= 2$, Cm $= 0.025$ g $\cdot cm^2$, and Car $= 15\ \mu g \cdot cm^2$).

and observation perturbation. It follows a normal (Gaussian) distribution

$$\varepsilon \sim \mathcal{N}(0, \sigma_\varepsilon^2 I) \quad (6)$$

where σ_ε^2 is the variance of the noise assumed unknown and I is the identity matrix of the same dimension as the vector R (i.e., nine). The vector of unknown parameters is, therefore, $\phi = (\theta^{(1)}, \theta^{(2)}, \theta^{(3)}, \theta^{(4)}, \sigma_\varepsilon^2)$, to be estimated using MCMC. In order to determine the *a posteriori* probability of the unknown parameters, it is necessary to define *a priori* distributions that well characterize the model. In our case, as there is no any auxiliary information, all the unknown vegetation parameters are assumed to follow uniform distributions $\theta^{(i)} \sim U_{\Theta^{(i)}}$ when $\theta^{(i)}$ is the discrete space of variation of $\theta^{(i)}$ defined in Table IV.

The mesophyll structure is assumed to be spatially homogeneous and to only vary with time in link with the phenological stage. Contrarywise, Cab, Cw, and LAI are known to vary between trees; thus, $\{\theta^{(2)}, \theta^{(3)}, \theta^{(4)}\}$ must be estimated separately from a pixel s to another. s belongs to the set of the image pixels $\Omega = \{(i,j)\}_{i=1,..,N_r; j=1,..,N_c}$, when N_r and N_c are the number of rows and column, respectively. A subscript s is added to $\theta^{(2)}$, $\theta^{(3)}$, and $\theta^{(4)}$ to distinguish them. The parameter set to be estimated in this case is $\Theta = \{\theta_s^{(2)}\}_{s \in \Omega} \cup \{\theta_s^3\}_{s \in \Omega} \cup \{\theta_s^{(4)}\}_{s \in \Omega} \cup \{\theta^{(1)}\}$. Even though $\{\theta_s^{(2)}, \theta_s^{(3)}, \theta_s^{(4)}\}$ are estimated independently for each pixels, they are assumed to be slightly different between neighboring pixels. In this respect, each variable is assumed to follow a Markov random

field (MRF) in space. The mathematical formulation is given in Appendix A. Since the magnitude of the noise ε over our set of observation is not well known, the corresponding variance is assumed unknown and follows the inverse gamma distribution $\sigma_\varepsilon^2 \sim IG(\alpha, \beta)$, where α and β are, respectively, the shape (height control) and the scale (propagation control) parameter of this distribution. Thus, the vector of constant parameters is $\psi = (\Theta^{(1)}, \Theta^{(2)}, \Theta^{(3)}, \Theta^{(4)}, \alpha, \beta)$. The derivation of the *a posteriori* probability of the unknown parameters is included in Appendix A.

Temporal regularization condition: Due to the short-time revisit of Sentinel-2 satellite, it is possible to account for time dependence in the implementation of the inversion procedure. As tree properties vary continuously in time, a Markov chain is deemed appropriate. The inversion is then operated by considering all images over the whole period. We use here the same annotations as the spatial variation with nevertheless some little changes considering the variance of the noise $\sigma_\varepsilon = \{\sigma_{\varepsilon,k}\}_{k=1,..,K}$, where K is the times series length and k is the image index within the series. The set of the image pixels, Ω, is extended in this case to take into account the time variation; $\Omega = \{(i, j, k)\}_{i=1,..,N;j=1,..,M;k=1,..,K}$. LAI, Cab, and Cw are varying in space and time. All of them are defined over the new space Ω. However, as in the case of a spatial regularization, these parameters remain close on a delimited space and are modeled as a spatiotemporal MRF. To symbolize the mesophyll structure, temporal variation, a subscript k is added to $\theta_k^{(1)}$, further estimated as $\{\theta_k^{(1)}\}_{k \in \Omega_k}$ with $\Omega_k = \{1, \ldots, k\}$. Since the temporal variation is slow, a Markov Chain is appropriate to describe the sequence of possible events $\theta_k^{(1)}$. The different steps to calculate the *a posteriori* probability of the unknown parameters are described in Appendix B.

D. LAI Ground-Truth Derivation Protocol

LAI measurements within each crown (LAI_{tree}) were carried out by using the relationship between light transmittance and LAI, described by the Beer–Lambert law [44]. T, the tree crown transmittance, is the ratio of the intensity reacting the ground surface (I) to the total intensity (I_T). This ratio is the gap fraction at ground level [P_{gap} [45], shown in (7)]

$$T(\theta) = \frac{I}{I_T} = \exp(-k(\theta) \times (\text{LAI}_{\text{tree}})) = P_{\text{gap}} \qquad (7)$$

where θ is the viewing angle, k is the extinction coefficient, depending on the leaf angle distribution, and LAI_{tree} is the LAI. To use these equations, a constant viewing angle and a homogeneous environment are required. Hence, to compute the gap fraction, first, a classification is needed to extract the sky pixels; then, a ring-based image division is required to ensure a constant value of leaf interception efficiency (i.e., k); finally, due to clumping effect, a patch-based image division is necessary to ensure homogeneity as it is required to use (7).

Olive trees are considered planophyle in terms of leaf inclination distribution [46]. In this case, k varies as a function of the viewing angle.
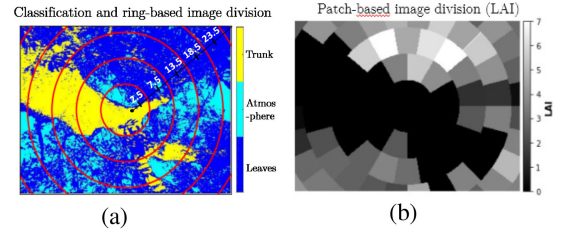

Fig. 7. Classification and Ring/Patch-based image division. (a) Smartphone image classification and ring-based division, where class 1 corresponds to foliage tissue, class 2 corresponds to areas of gaps, and class 3 corresponds to trunk and (b) LAI patches.

In order to use (7), we first need to eliminate the woody materials in the aim to not overestimating LAI_{tree}. Each image is separated into foliage tissue, woody materials, and areas of gaps, as shown in Fig. 7(a), using an image classification algorithm, i.e., the GMM [47]. Second, to ensure that the k value remains almost constant, we divided the image into six rings [see Fig. 7(a)] with different zenith angles varying from $5°$ to $30°$ (camera maximum view angle). The corresponding k values for each ring are $k_{\text{ring}} = \{0.8051, 0.8060, 0.8077, 0.8104, 0.8144, 0.8197\}$. They are calculated using the SAIL model [48]. Finally, due to clumping effect, the leaves spatial distribution is not homogeneous by rings, which can cause an underestimation of the LAI [49]. Therefore, the rings are divided in homogeneous patches, as shown in Fig. 7(b).

After subtracting the trunk pixels $N_{\text{patch}^{\text{trunk}}}$ from the total patch pixels N_{patch}, the gap fraction per patch can be computed by dividing the number of gap pixels $N_{\text{patch}^{\text{gap}}}$ by N_{patch}. Then, using (7), the corresponding $\text{LAI}_{\text{patch}}$ is derived [see Fig. 7(b)]

$$\text{LAI}_{\text{patch}} = \frac{-1}{k_{\text{ring}}} \ln \left(\frac{N_{\text{patch}^{\text{gap}}}}{N_{\text{patch}} - N_{\text{patch}^{\text{trunk}}}} \right) \qquad (8)$$

and the image LAI is obtained averaging all the patches.

Finally, LAI_{tree} for the whole tree crown is calculated in averaging the LAI of the eight images (one sample is shown in Fig. 7).

In our case, we need to calculate $\text{LAI}_{\text{total}}$ in the surface area $S_{\text{total}} = 24 \text{ m} \times 24 \text{ m}$. It is derived from LAI_{tree} as follows:

$$\text{LAI}_{\text{total}} = \text{LAI}_{\text{tree}} \times \frac{S_{\text{tree}}}{S_{\text{total}}} \qquad (9)$$

where S_{tree} is the tree crown horizontal surface. To be measured for each individual tree, the perimeter of the tree crown's orthogonal projection was marked on the soil surface with a pole fitted with an eight-point leveling bubble, drawing eight equidistant transects from the tree center. The olive crown area projected into the horizontal plane was determined as the sum of the circular sector areas for each transect [50].

V. EXPERIMENTAL RESULTS

A. Pretreatment

1) Sharpening: Results of the fusion between Sentinel-2 and Planet images are shown in Fig. 8 on a subset located in field 1.
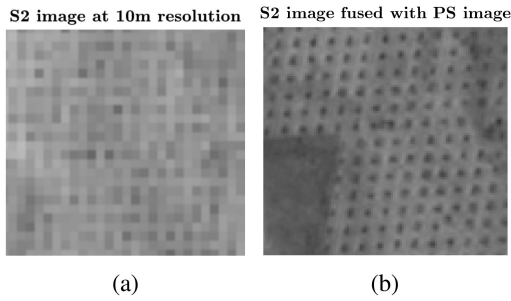
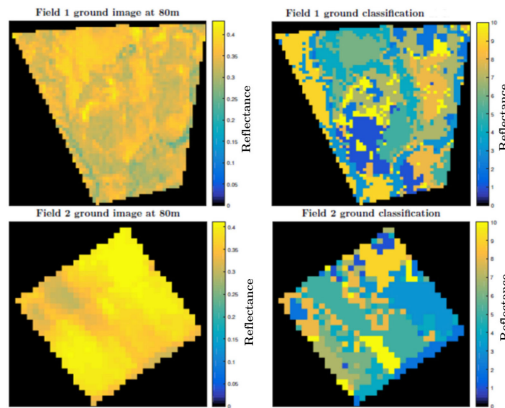Fig. 8. Sentinel-2 image at (a) 10 m and (b) fused with the Planet image.

Fig. 9. Soil background detection and classification for fields 1 and 2.

Fig. 8(b) reveals the asset of this merging in terms of image definition compared to the Sentinel-2 image [see Fig. 8(a)].

2) Soil Image Downsampling: The soil image is resampled to 80-m resolution to estimate the background reflectance pixel by pixel (see Fig. 9). The soil classification into ten classes seems to be justified. What seems to be an overclassification is nevertheless required because the class centers are the sole soil background reflectances simulated by DART.

B. Monodate

1) LUT and MCMC Validation: Results obtained from the LUT and the MCMC inversion for both fields on June 21, 2019 are presented in Figs. 10 and 11, respectively, whereas, for those in 2020 and 2021, they are omitted since the visual difference between maps is rather small. One can see that the entire *a priori* ranges were covered by the estimated values for all the biophysical parameters but with different occurrence probability as particular trees are shown. A visual check with the Sentinel-2 fused image at 3-m resolution reveals that low estimates of LAI and Cab correspond to senescent trees. A thorough visual inspection of these maps shows that high LAI pixels have a low variability in Cab, whereas pixels with low LAI present a wide range of Cab values especially in field 2. This reflects that in the latter case, the sensitivity to Cab becomes minimal that increases the estimation variance [51]. The output map properties of the LUT inversion approach are shown in Figs. 10(a) and 11(a), whereas output map properties of the MCMC inversion approach

are shown in Figs. 10(b) and 11(b). The Cw estimate is noisier than the LAI and Cab maps, which could explain by the low sensitivity of Sentinel-2 measurement to water content (except B11 band). The estimates of LAI, Cab, and Cw were compared with the collection of 16 ground measurements for the two sites. Table V displays the results of model inversion to the groups' ground measurements using LUT, MCMC, and MCMCtimeseries inversion techniques, while Table VI indicates the accuracy of each one. For MCMCtimeseries inversion results, they will be discussed in Section V-C. The LAI was estimated more accurately, followed by Cab and then by Cw. It shows that both LUT and MCMC inversion methods globally support the same acceptable accuracy on retrieved properties [19], [36]. The LAI shows a lesser bias and a higher correlation than the others parameters because the observations are highly sensitive to this parameter. The bias of Cab and Cw may be explained by the fact that satellite observations are primarily impacted by the top layer of the canopy where sunlit leaves are located. These latter are more subject to stress than any other layer of the canopy [52], [53]. For the structural parameter N, the estimated value equals $N = 2.5$ for both fields 1 and 2. This value is around the known values for olive trees [54]. As for the estimated noise, starting from the *a priori* value and after a number of iterations, the estimated parameter oscillates around average values, which are the most likely, $\sigma_\varepsilon \approx 0.005$ and 0.0024 for fields 1 and 2, respectively. These values sound reasonable for Sentinel-2 MSI [55]. Visual inspection shows that results are more homogeneous with the MCMC method. Indeed, as the sensitivity to Cab and Cw is not too high, it was important to reduce the spatial variation in order to decrease uncertainty. The comparisons with the field measurements prove the quality of the estimated products by using the MCMC monodate inversion, where the smooth biophysical parameter variations in space as reported in earlier studies are taken into account [42]. Precision of the retrieval mainly depends on the satellite data quality. Although the radiometric signal coming from tree is lower than the one issued from the soil background, it was possible to retrieve the set of parameters with an acceptable level of accuracy particularly for LAI estimates ranging from 0 to 0.14 [56]. This performance was possible thanks to the sensitivity of Sentinel-2 spectral bands to the vegetation properties with appropriate narrow bands in RE and shortwave-infrared band, the precise soil signature detection obtained by Sentinel-2 and Planet image fusion, the precise RTM (DART), and the accurate inversion method.

2) Reflectance Spectra Analysis: In order to better understand the effect of the vegetation on the reflectance spectrum, the difference between soil and soil plus trees is analyzed. Results shown in Fig. 12 relate to the four measurement groups in June 2019, where each image is of size $80 \times 80 \text{ m}^2$ and contains around 11 olive trees, four from which were measured and their mean corresponds to one measurement group. The latter plots them at 3-m resolution for S4 band (red), and Fig. 13 displays the corresponding reflectance spectra. In addition to the soil and the total Sentinel-2 80-m spectra, here, two additional spectra simulated by DART with parameters estimated by LUT and MCMC are shown for the sake of comparison. Moreover, for better
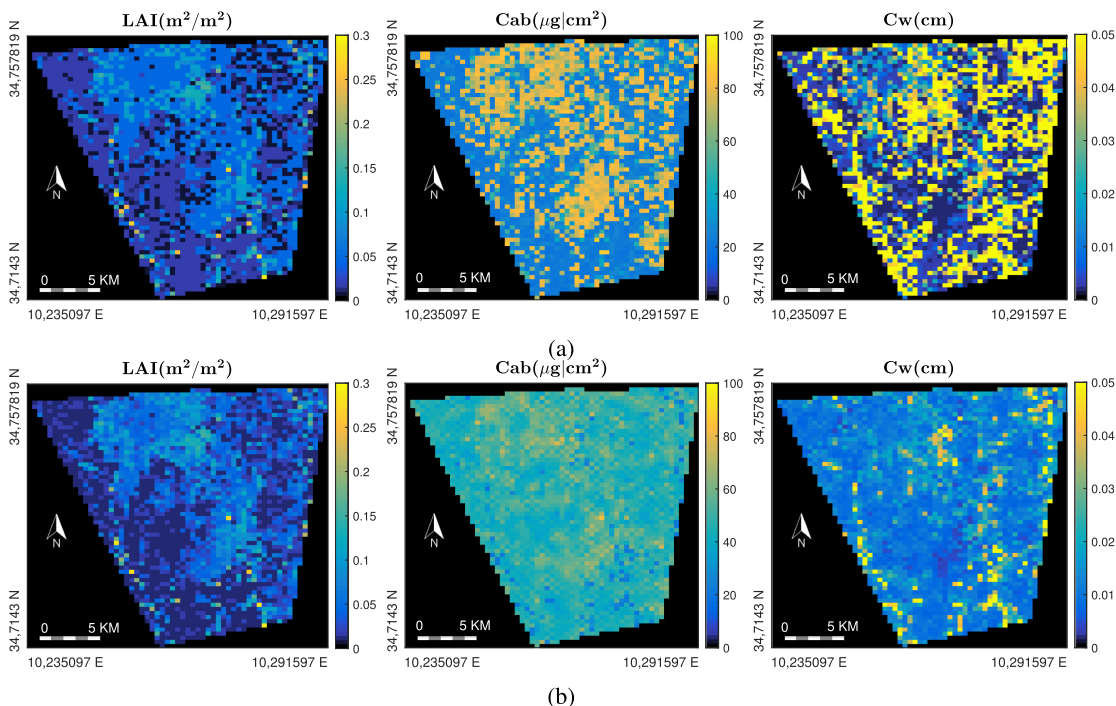
Fig. 10. Field 1 map properties at 80 m for (a) LUT inversion and (b) MCMC inversion.
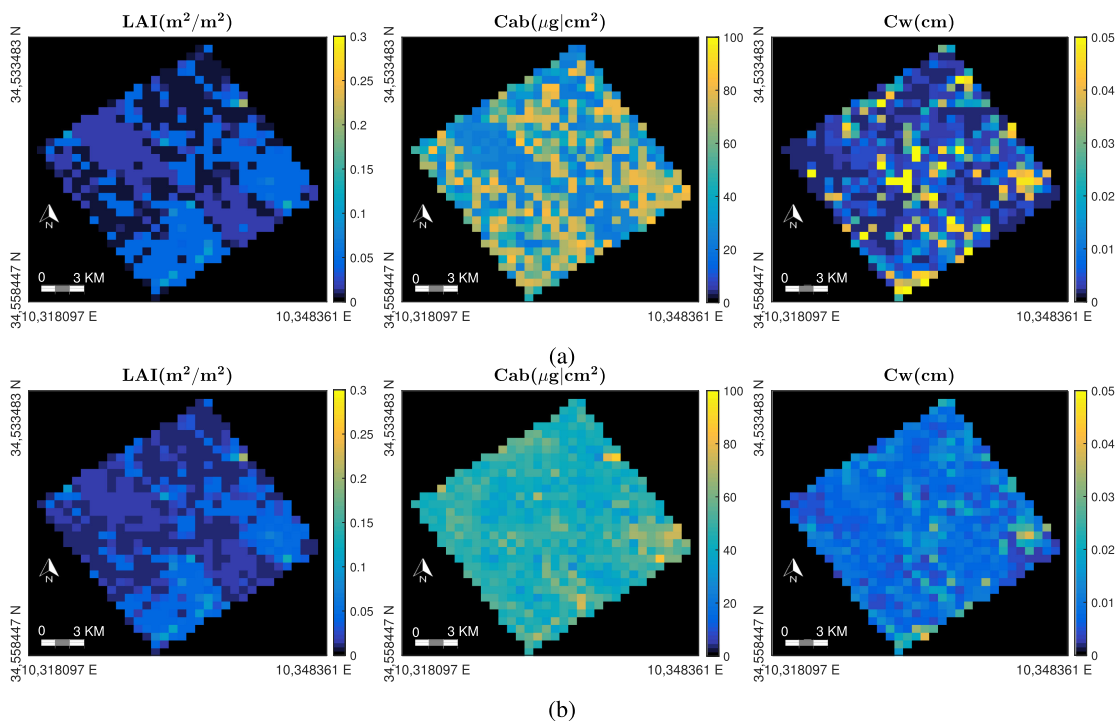

Fig. 11. (a) and (b) Idem as Fig. 10 for field 2.

distinguishing between the different spectra, a zoom around the S4 band is shown. In the visible spectrum, the vegetation reflectance response is mainly governed by the quantity of Cab, while in the NIR domain, it is due to LAI and leaf structure N. In the SWIR domain, the sensitivity to the water content Cw dominates [57]. In our case, since the 80 m Sentinel-2 pixels are mixed, the spectral response of Sentinel-2 combines the olive trees and the soil components. As our field soil is too bright, the highest reflectance values belong to the soil class image in all the spectral bands for all the field groups. Comparison

TABLE V
COMPARISON OF THE LAI, Cab, AND Cw ESTIMATED VALUES USING LUT, MCMC, AND MCMCTIMESERIES WITH THE GROUND MEASUREMENTS

Group	LAI				$Cab(\mu g|cm^2)$				$Cw(g.cm^{-2})$			
	measured	LUT	MCMC	MCMC timeseries	measured	LUT	MCMC	MCMC timeseries	measured	LUT	MCMC	MCMC timeseries
Dev1june19	0.1208	0.1083	0.1158	0.1169	54.1833	81	56.14	69	0.0198	0.0274	0.0157	0.0179
Senes1june19	0.0392	0.0405	0.0302	0.0362	55.95	76	55.3	40	0.0147	0.0159	0.007	0.0057
Dev1july20	0.1343	0.1092	0.1125	0.12	63.20	80	61.28	64.2	0.0182	0.0283	0.0128	0.0099
Senes1july20	0.0129	0.01387	0.0133	0.012	28.3387	22	43.4	30.2	0.0178	0.00499	0.00955	0.01364
Dev11janu21	0.1108	0.1308	0.1253	0.1133	54.66	76	54.86	58.6	0.0147	0.00865	0.01179	0.02774
Senes11janu21	0.0119	0.0155	0.01487	0.0092	56.3257	49	52	60	0.0182	0.002	0.01007	0.006584
Dev12janu21	0.0452	0.0506	0.0486	0.0434	55.558	51	56.4	64.4	0.0147	0.05	0.03477	0.01966
Senes12janu21	0.0186	0.0365	0.0219	0.0157	52.93	25	49.88	30	0.0182	0.00299	0.0135	0.008822
Dev2june19	0.1212	0.09672	0.1013	0.1050	49.5427	81	75.64	56	0.0162	0.01159	0.0141	0.0149
Senes2june19	0.0174	0.0155	0.0152	0.0156	50.8867	23	37.32	23.2	0.0139	0.00432	0.0084	0.0087
Dev2july20	0.0804	0.1067	0.0910	0.0865	55.5850	82	68.48	59.6	0.0158	0.01389	0.0144	0.01663
Senes2july20	0.01	0.0126	0.009	0.0095	24.6966	21	35.8	24	0.0111	0.00399	0.0091	0.0094
Dev21janu21	0.1144	0.1023	0.1022	0.1092	48.7369	34	40.74	49	0.0139	0.025	0.0161	0.01978
Senes21janu21	0.0115	0.0145	0.01433	0.0088	39.75	20	42.64	28	0.0111	0.0349	0.009362	0.00744
Dev22janu21	0.1103	0.1023	0.1055	0.1069	57.8636	84	60.58	59.8	0.0139	0.0274	0.01674	0.01475
Senes22janu21	0.0154	0.0102	0.01283	0.0141	22.66	26	50.88	22.8	0.0111	0.002	0.008519	0.00929

TABLE VI
COMPARISON OF THE LUT, MCMC, AND MCMCTIMESERIES INVERSION METHOD ACCURACY IN RETRIEVING LAI, Cab, AND Cw VALUES

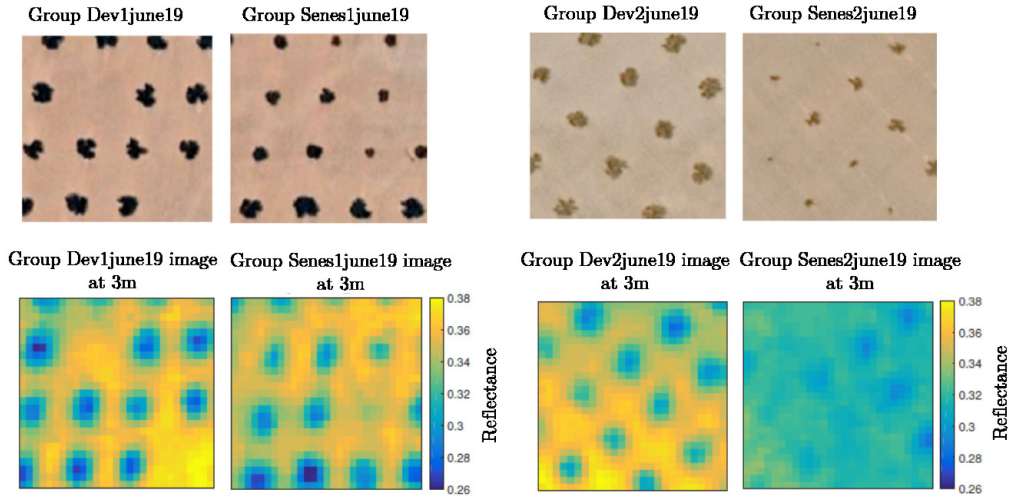| Inversion method	LAI			$Cab(\mu g|cm^2)$			$Cw(g.cm^{-2})$		
	Bias	RMSE	R^2	Bias	RMSE	R^2	Bias	RMSE	R^2
LUT	0.0005	0.0139	0.9678	-3.7583	20.4236	0.8309	-0.0001	0.0081	0.7163
MCMC	0.0025	0.0098	0.9842	-4.4046	12.0156	0.9415	0.00092	0.0047	0.9067
MCMC timeseries	0.0033	0.0062	0.9937	2.0042	11.6617	0.9449	0.00098	0.0041	0.9278

Fig. 12. Images of the four groups of validation: first and second columns correspond to Google Earth image and S4 band of Sentinel-2 at 3-m resolution, respectively.

between the inverted spectra (LUT and MCMC) and the original reflectance shows close results. Even if the inverse model remains ill-posed, these close results are reached with accurate soil estimation, which is a driving signature, accurate 3-D canopy modeling using DART, and finally accurate inversion method. Difference between soil and soil+tree spectra is the highest for group Dec1june19 and Dev2june19. Conversely, for group Senes2june19, they are close to each other. This difference is dependent on the tree development and particularly the LAI value. This is evidenced in Fig. 12, where trees are clearly distinguishable in group Dev1june19 but not in group Senes2june19. This explain the feasibility of LAI estimation in the range between 0 and 0.14 using reliable satellite data (Sentinel-2) for accurate global and soil signature estimate. Due to the brightness increase of the soil as a function of the wavelength, the global reflectance is also increasing even if vegetation reflectance decreases in red spectrum due to the chlorophyll absorption. It remains that vegetation effect in S4 (red) is well observed for all the groups, where difference between soil background and the global reflectance increases. The latter effect is dependent not only on Cab but also on LAI. Hence, the more leaves the more absorption due to chlorophyll is observed. As Cab × LAI shows the highest
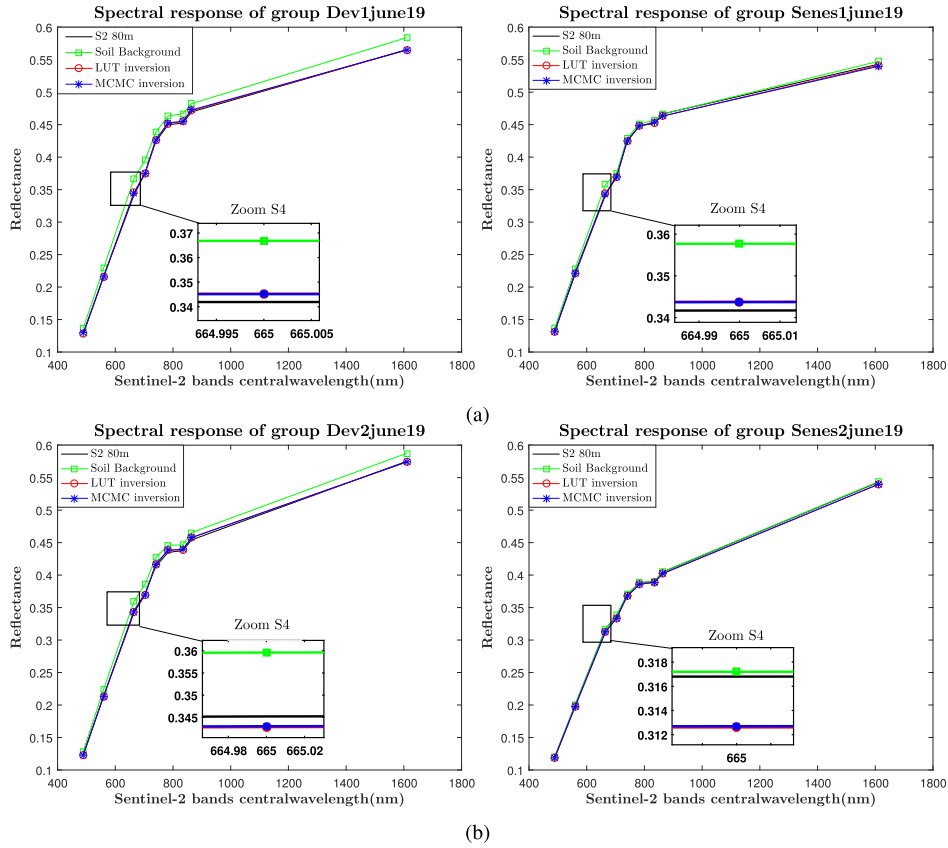
Fig. 13. Reflectance spectra for (a) field 1 and (b) field 2 ground measurement groups.
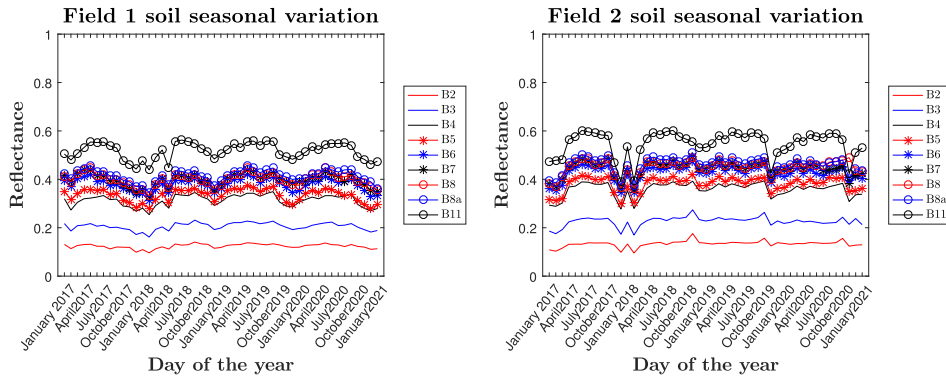

Fig. 14. Field 1 and field 2 soil seasonal variation during the period (2017–2021).

values for groups Dev1june19 and Dev2june19, the curve differences in S4 are the highest in these cases. Water content has similar effect like the chlorophyll, but in the shortwave infrared domain (S11), soil and soil+trees curves are the furthest in this domain for group Dev1june19 since the product LAI $\times$ Cw is the highest.

C. Time Series

1) Seasonal Variation: Our goal is to capture the development of olive tree growth using the Sentinel-2 image time series

over an entire season and then compare different seasons. These time series allow monitoring with precision the temporal dynamics of the biophysical properties of the sampled fields with the in fine objective to give raise to the more important phenomena such as the segregation of rainy periods, flowering, and pruning. LUT, MCMC date-by-date, and MCMC time-series (called in the following MCMCtimeseries) inversion are performed over the whole set of Sentinel-2 dates (around four years). This requires the estimation of the soil reflectance within the studied fields all along the time series. Fig. 14 draws the seasonal variations of the soil, and Fig. 15 plots the development cycle of
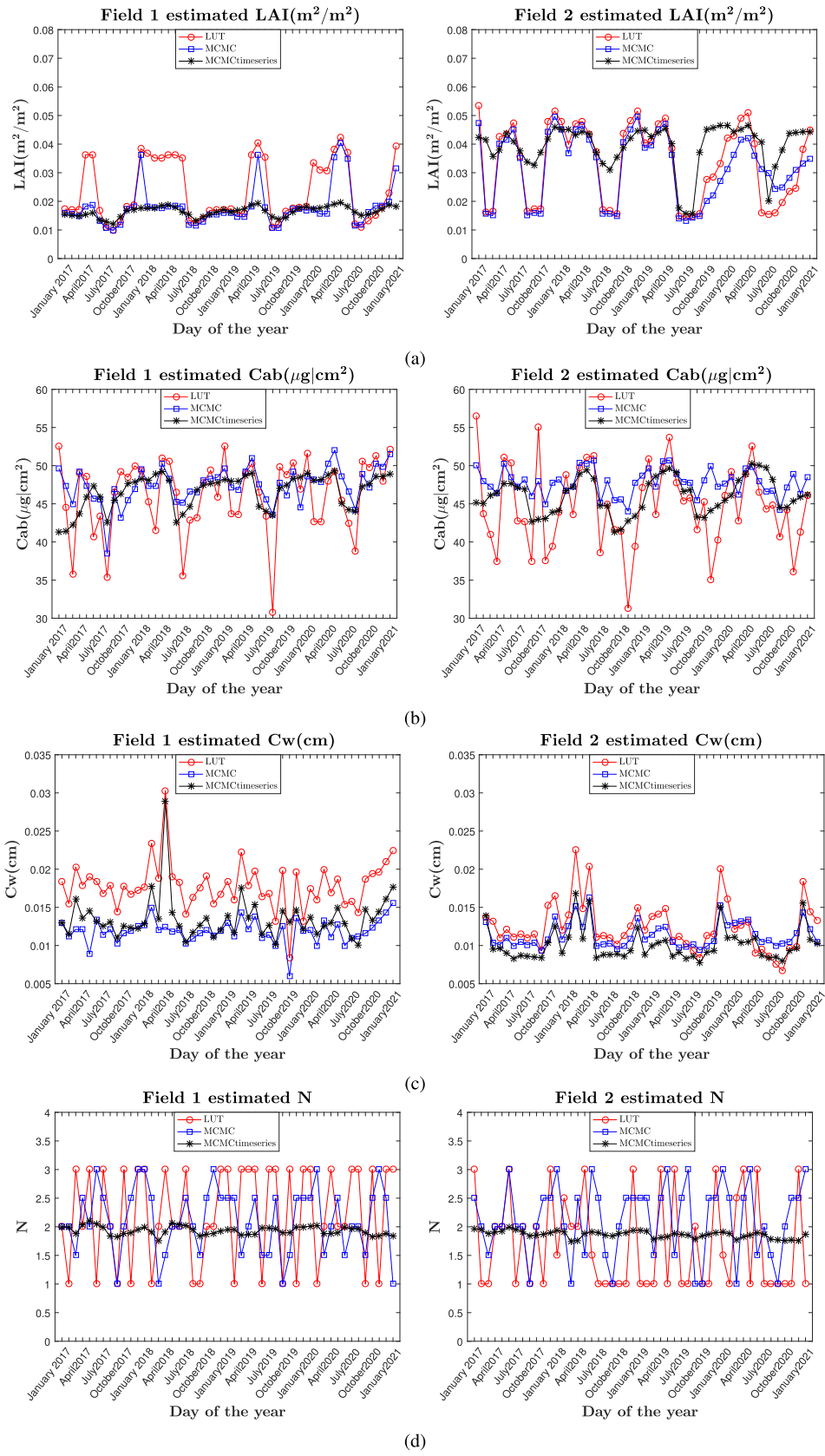
Fig. 15.   Field 1 and field 2 estimated properties in the period (2017–2020): (a) LAI, (b) Cab, (c) Cw, and (d) N.

the olive trees in the Châal area in terms of biophysical property variations. For the soil plot, as expected, Fig. 14 shows that the field 2 soil spectral response for all Sentinel-2 bands is higher than the field 1 soil spectral response due to soil composition (field 1: marginal soil; field 2: sandy soil). These different soil compositions under the same rainfall range show a highly meaningful effect on the values of the biophysical parameters, especially on LAI. In fact, on a deep sandy soil (field 2), the LAI average is around 0.04, whereas on a marginal soil (field 1), it is only around 0.02. We noticed an increase of the soil reflectance from the end of February to September, which corresponds to the hot and dry seasons leading to get a bright soil. In addition, during this period of the year, the sun elevation is high and the hot spot effect may be captured. As a remind, this phenomenon marked by a surge of reflectance in all spectral bands is observed when the illumination and the scanning directions coincide due to the lack of observed shadows, whereas all sunlit areas are seen [49]. The decrease until the end of the year is possibly due to the presence of an understory layer formed by grassland laying over wet soil since rainfall events occurred. Shadowing effect may even enhance this feature. The remaining plots fit well the expected seasonal variations of the biophysical properties of the olive trees. In particular, Fig. 15(a) shows that LAI decreases around the end of January, which corresponds to the pruning season performed between end of winter and flowering [58], and increases from March to reach a peak by the end of April due to the flowering season [59]. Finally, the LAI decreases from June, when the majority of old leaf and petals starts falling in August and increases again until the end of the year. A comparison between the two fields of LAI shows that the highest values occur during the second growing period. This is confirmed by ground truth where the trees are clearly more developed during the post-summer period. From Fig. 15(b), Cab gets its largest value in May corresponding to the flowering season. In June, when rainfall becomes scarce, Cab values drop significantly [60]. From Fig. 15(c), one can see that Cw is maximum during the autumn and winter seasons due to rainfall. Besides, Cw shows a slight variation throughout the year, within a range around 0.013 cm. This almost invariance could be explained by the low sensitivity of the measure to the water content. The estimated parameter N [see Fig. 15(d)] shows an average value around 2 throughout the year. It decreases slightly during two periods of time: the end of February and the end of September. This behavior is connected to the apparition of new leaves having small N values in these times [61]. Olive leaves have a cycle of two years. Hence, leaves with different ages and having different N values coexist. This explains the low temporal variability of N. For that, we think that the N parameter is less relevant for monitoring the olive growth than LAI.

Regarding the annual variations, a same seasonal trend is noticed during the four recorded years. However, some differences are detected relatively to the estimated values of the biophysical parameters. This is caused by the water shortage and the drought during 2017 with an annual average equals to 149.06 mm [62]. LAI, Cab, and Cw reached their lowest values in 2017. The most significant peaks of LAI were detected in

2018 and 2019, especially in April 2019 (0.0189, 0.0451) in fields 1 and 2, respectively, using the MCMCtimeseries method. Fig. 15(b) shows mainly similar values for Cab especially in April 2019: 48 and 49 μg/cm^2 in fields 1 and 2, respectively, using the MCMCtimeseries method. For estimated values of Cw using the MCMCtimeseries method, the majority of highest values occurs also in 2018 and 2019. This can be explained by the positive influence on the tree development during the winter's heavy rainfall events with an annual average of 179.04 and 211.83 mm for 2018 and 2019, respectively [62].

Taking into account the spatial and the temporal variations, MCMCtimeseries inversion shows a smoother plot for all the estimated biophysical parameters, presenting more realistic results since the biophysical properties are not so fluctuating in time. For example, it is impossible to obtain a variation from 0.0147 (September 2019) to 0.0487 (October 2019) in terms of LAI during one month in field 2 using the LUT and the MCMC date-by-date inversion, as shown in Fig. 15(a). The temporal biophysical profiles match with results found in the literature about the description of the phenological growth stages of olive tree [59]. LAI and Cab estimates follow the same behavior. Furthermore, the presence of water has both direct and indirect influences on all biophysical parameters. Particularly, rain is very important for olive tree, especially since the Châal fields are not irrigated and depend entirely on rainfall contribution. Trend of biophysical parameters over the seasons and the years could be further exploited to measure the impact of climate change on the ecophysiology of olive tree orchards in regard to its strong socioeconomical role. Furthermore, since high-quality Sentinel-2 time series are freely distributed, the method proposed here could serve to a fine monitoring of a very popular crop serving for proxy to detect tree diseases and also prevent any early unexpected senescence. In conclusion, comparing the MCMCtimeseries inversion with the previous inversion techniques, such modeling allows reducing the atmospheric effects and the sensor noise in the inversion and, therefore, improves the quality of the results at the end.

2) MCMCtimeseries Validation: In order to validate results improvement brought by the MCMCtimeseries inversion, output maps of canopy properties are presented in Fig. 16 based on field measurements acquired in June 2019. Visual inspection shows that results are less noisy compared to MCMC and LUT; this is mainly the case for LAI.

The MCMCtimeseries inversion approach (see Tables V and VI) provides more realistic estimated parameters and lower values of RMSE and R^2. Hence, the improvement of the MCMCtimeseries inversion compared to the MCMC inversion at a given time proves the importance of taking into account the spatiotemporal regularization.

VI. Conclusion

In this study, we evaluated the capability of the multispectral Sentinel-2 imagery completed by Planet imagery to obtain a mapping of LAI, Cab, Cw, and N variables in two open olive tree orchards of the Châal area in Tunisia that differ in soil
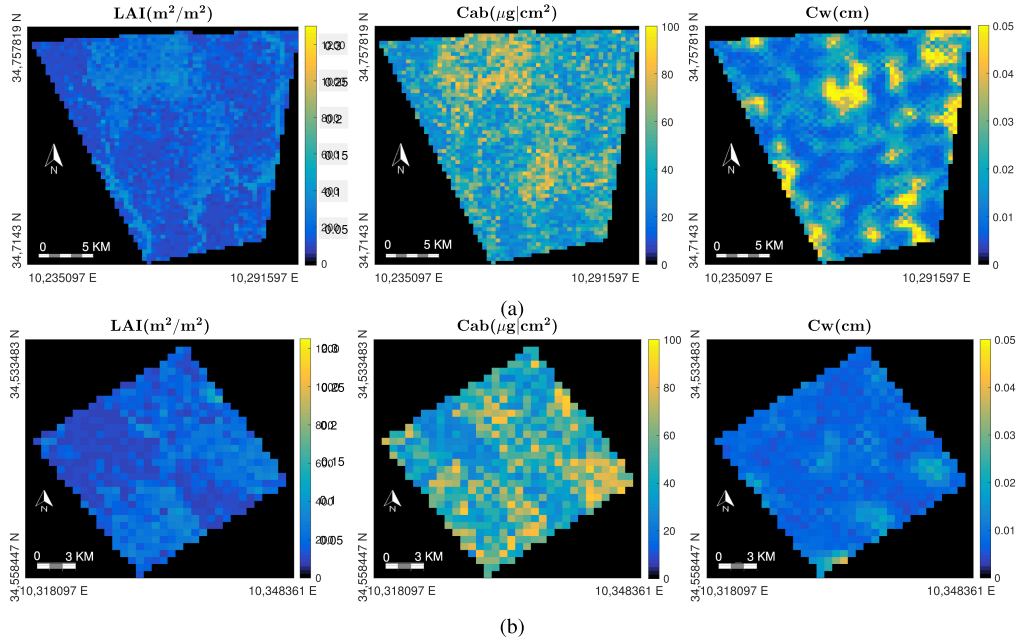
Fig. 16. Map properties using the MCMCtimeseries approach for (a) field 1 and (b) field 2.

types. The method relies on the inversion of the 3-D radiative transfer DART model, using the LUT technique, and an original approach based on the MCMC technique. This latter includes spatial and temporal regularization, MCMCtimeseries. Overall results reveal the appropriateness of the DART model for simulating the canopy reflectance of Sentinel-2 bands and to retrieve the most relevant olive tree biophysical properties using the MCMC inversion technique. It comes out that the Cab and Cw retrieval accuracy is affected by the limits of the RTM to describe multiscale processes and the definition of the Sentinel-2 bands in regard to their central wavelength and width. Further improvement for biophysical parameters retrieval is expected by combining Sentinel-2 and Sentinel-3 data as this latter owns spectral bands dedicated to measure the pigment contents contained in olive tree leaves e.g., the Sentinel-3 OLCI Terrestrial Chlorophyll Index for Chlorophyll retrieval [63]. The MCMCtimeseries inversion approach could be improved by relaxing the temporal dependence in case of strong change due to rainfall, pruning, flowering, etc.

The validation strategy is the cornerstone of the whole approach. The protocol to collect multiscale and multidate field measurements is somewhat cumbersome and must be considered here as a demonstrator. In the future, it is clear that it should be repeated at the landscape scale to emphasize the usefulness of the method for olive crop monitoring.

APPENDIX A
DERIVATION OF THE POSTERIOR PROBABILITY (SPATIAL VARIATION)

The a prior probability derived using the Bayes theorem is

$$P(\phi|R,\psi) \propto P(R|\phi,\psi)P(\phi)$$

$$\propto \prod_s P(R_s|\phi,\psi)P(\phi)$$

$$\propto \prod_s P(R_s|\phi,\psi)P(\theta)P(\sigma_\varepsilon^2) \qquad (10)$$

where

$$P(\phi) = P(\theta)P(\sigma_\varepsilon^2)$$
$$= P(\{\theta_s^{(2)}\}_{s\in\Omega})P(\{\theta_s^{(3)}\}_{s\in\Omega})P(\{\theta_s^{(4)}\}_{s\in\Omega})$$
$$P(\{\theta^{(1)}\})P(\sigma_\varepsilon^2). \qquad (11)$$

And $\forall p \in \{2,..,4\}$

$$P(\{\theta_s^{(p)}\}_{s\in\Omega}) = \exp\left(-\beta_s \sum_{(s,s')\in C}(\theta_s^{(p)} - \theta_{s'}^{(p)})^2\right)$$
$$\prod_s \mathbb{1}_{\Theta^{(p)}}(\theta_s^{(p)}) \qquad (12)$$

where β_s is the spatial regularization parameter (i.e., the larger it is, the more regular the field), C is the neighbor set, and

$$C = \{(s,s') \in \Omega \times \Omega / s = (i,j), s' = (i',j'),$$
$$|i-i'| + |j-j'| = 1\} \qquad (13)$$

where $\mathbb{1}_{\Theta^{(p)}}$ is the indicator function and

$$\mathbb{1}_{\Theta^{(p)}}(x) = \begin{cases} 1, & \text{si} \quad x \in \Theta^{(p)} \\ 0, & \text{sinon} \end{cases}. \qquad (14)$$

Thus

$$P(\phi|R,\psi) \propto \prod_s P(R_s|\phi,\psi)$$
$$\times \left[\prod_{p=2}^{4}\prod_{(s,s')} \exp -(\theta_s^{(p)} - \theta_{s'}^{(p)})^2\right]$$

$$\times \left[\prod_{p=2}^{4} \prod_{s} \mathbb{1}_{\Theta^{(p)}}(\theta_s^{(p)}) \right]$$

$$\mathbb{1}_{\Theta^{(4)}}(\theta^{(4)}) \times P(\sigma_\varepsilon^2). \tag{15}$$

The Gibbs sampler is used then to calculate the *a posteriori* probability

$$P(\theta_s^{(p)} | \theta_{s' \neq s}^{(p)}, \theta_{s \in \Omega}^{(q \neq p)}, \sigma_\varepsilon^2, R, \psi)$$

$$= \frac{P(\phi | R, \psi)}{\sum_{x \in \Theta^{(p)}} P(\phi^{(x,p)} | R, \psi)} \tag{16}$$

where

$$\phi^{(x,p)}(i) = \begin{cases} \phi(i), & i \neq p \\ x, & i = p \end{cases}. \tag{17}$$

Thus, the probability of the θ_s^p parameter knowing its neighbor is as follows:

$$P(\theta_s^{(p)} | \theta_{s' \neq s}^{(p)}, \theta_{s \in \Omega}^{(q \neq p)}, \sigma_\varepsilon^2, R, \psi) =$$

$$\frac{P(R_s | \phi, \psi) \prod_{(s,s')} \exp - \left(\theta_s^{(p)} - \theta_{s'}^{(p)} \right)^2}{\sum_{x \in \Theta^{(p)}} P(R_s | x, \psi) \prod_{(s,s')} \exp \left(-(x - \theta_{s'}^{(p)}) \right)^2} =$$

$$\frac{\prod_{(s,s') \in C} \exp - \left(\theta_s^{(p)} - \theta_{s'}^{(p)} \right)^2 P(R_s | \theta_s^{(p)}, \theta_s^{(q \neq p)}, \theta_s^{(1)}, \sigma_\varepsilon^2, \psi)}{\sum_{x \in \Theta^{(p)}} \prod_{(s,s') \in C} \exp - \left(x - \theta_{s'}^{(p)} \right)^2 P(R_s | x, \theta_s^{(q \neq p)}, \theta_s^{(1)}, \sigma_\varepsilon^2, \psi)} =$$

$$\frac{\exp - \sum_{(s,s') \in C} \left(\theta_s^{(p)} - \theta_{s'}^{(p)} \right)^2 P(R_s | \theta_s^{(p)}, \theta_s^{(q \neq p)}, \theta_s^{(1)}, \sigma_\varepsilon^2, \psi))}{\sum_{x \in \Theta^{(p)}} \exp - \left(\sum_{(s,s') \in C} (x - \theta_{s'}^{(p)})^2 \right) P(R_s | x, \theta_s^{(q \neq p)}, \theta_s^{(1)}, \sigma_\varepsilon^2, \psi))} =$$

$$\frac{\exp - \sum_{(s,s') \in C} \left(\theta_s^{(p)} - \theta_{s'}^{(p)} \right)^2 - \frac{\|f(\theta_s) - R_s\|^2}{2\sigma_\varepsilon^2})}{\sum_{x \in \Theta^{(p)}} \exp \left(- \sum_{(s,s') \in C} \left(x - \theta_{s'}^{(p)} \right)^2 - \frac{\|f(\theta_s^{(x,p)}) - R_s\|^2}{2\sigma_\varepsilon^2} \right)} \tag{18}$$

where

$$\theta_s^{(x,p)}(i) = \begin{cases} \theta_s(i) \ \forall i \neq p \\ x, \quad i = p \end{cases}. \tag{19}$$

Regarding the estimated $\theta^{(1)}$ parameter, its *prior* follows a uniform distribution $\theta^{(1)} \sim U_{\Theta^{(1)}}$

$$P(\theta^{(1)} | \phi \setminus \{\theta^{(1)}\}, R, \psi) \propto$$

$$P(R | \theta^{(1)}, \phi \setminus \{\theta^{(1)}\}, \psi) \mathbb{1}_{\Theta^1}(\theta^{(1)}) \propto$$

$$\prod_{s} P(R_s | \theta^{(1)}, \phi \setminus \{\theta^{(1)}\}, \psi) \mathbb{1}_{\Theta^1}(\theta^{(1)}) \propto$$

$$\frac{1}{\sqrt{2\Pi}\sigma_\varepsilon^2}^{\frac{(NLK)}{2}} \exp \left(- \frac{\sum_s \|f(\theta_s) - R_s\|^2}{2\sigma_\varepsilon^2} \right)$$

$$\mathbb{1}_{\Theta^1}(\theta^{(1)}). \tag{20}$$

Finally, σ_ε^2 is estimated as

$$P(\sigma_\varepsilon^2 | \phi \setminus \{\sigma_\varepsilon^2\}, R, \psi) \propto$$

$$P(R | \sigma_\varepsilon^2, \phi \setminus \{\sigma_\varepsilon^2\}, \psi) P(\sigma_\varepsilon^2) \propto$$

$$\prod_{s} P(R_s | \sigma_\varepsilon^2, \phi \setminus \{\sigma_\varepsilon^2\}, \psi) P(\sigma_\varepsilon^2) \propto$$

$$\frac{1}{\sqrt{2\Pi}\sigma_\varepsilon^2}^{\frac{(N_b N_r N_c)}{2}} \exp \left(- \frac{\sum_s \|f(\theta_s) - R_s\|^2}{2\sigma_\varepsilon^2} \right)$$

$$P(\sigma_\varepsilon^2) \propto$$

$$IG \left(\alpha + \frac{N_b N_r N_c}{2}, \frac{\sum_s \|f(\theta_s) - R_s\|^2}{2} + \beta \right). \tag{21}$$

APPENDIX B
DERIVATION OF THE POSTERIOR PROBABILITY (TEMPORAL VARIATION)

The *a priori* probability derived using the Bayes theorem is then

$$P(\phi | R, \psi) \propto P(R | \phi, \psi) P(\phi)$$

$$\propto \prod_{s} P(R_s | \phi, \psi) P(\phi)$$

$$\propto \prod_{s} P(R_s | \phi, \psi) P(\theta) P(\sigma_{\varepsilon,k}^2) \tag{22}$$

where

$$P(\phi) = P(\theta) P(\sigma_{\varepsilon,k}^2)$$

$$= P(\{\theta_s^{(2)}\}_{s \in \Omega}) P(\{\theta_s^{(3)}\}_{s \in \Omega}) P(\{\theta_s^{(4)}\}_{s \in \Omega})$$

$$P(\{\theta_k^{(1)}\}_{k \in \Omega_k}) P(\sigma_{\varepsilon,k}^2). \tag{23}$$

And $\forall p \in \{2, .., 4\}$

$$P(\{\theta_s^{(p)}\}_{s \in \Omega}) =$$

$$\exp \left(- \sum_{\substack{(s,s') \in C \\ k=k'}} \beta_s^{(p)} (\theta_s^{(p)} - \theta_{s'}^{(p)})^2 \right)$$

$$\exp \left(- \sum_{\substack{(s,s') \in C \\ k \neq k'}} \beta_t^{(p)} \sqrt{t_k - t_{k'}} (\theta_s^{(p)} - \theta_{s'}^{(p)})^2 \right) \times$$

$$\prod_{s \in \Omega} \mathbb{1}_{\Theta^{(p)}}(\theta_s^{(p)}) \tag{24}$$

where C is the neighbor set $C = \{(s, s') \in \Omega \times \Omega\}$, and

$$\left. \begin{array}{l} s = (i, j, k) \\ s' = (i,' j,' k') \end{array} \right\} \begin{array}{l} |i - i'| + |j - j'| = 1, k = k' \\ |k - k'| = 1, i = i,' j = j'. \end{array} \tag{25}$$

For $p = 1$

$$P(\{\theta_k^{(p)}\}_{k \in \Omega_k}) =$$

$$\exp \left(- \sum_{\substack{(k,k') \in C_k \\ k \neq k'}} \beta_t^{(p)} \sqrt{t_k - t_{k'}} (\theta_k^{(p)} - \theta_{k'}^{(p)})^2 \right)$$

$$\mathbb{1}_{\Theta^{(p)}}(\theta_k^{(p)}) \tag{26}$$

where $C_k = \{(k, k') \in \Omega_K \times \Omega_K, |k - k'| = 1\}$ is the set of temporal neighbors for the parameter $\theta_k^{(1)}$. Thus

$$P(\phi | R, \psi) \propto$$

$$\prod_{s} P(R_s | \phi, \psi)$$

$$\left[\prod_{\substack{p=2 \\ k=k'}}^{4}\prod_{(s,s')}\beta_s^{(p)}\exp\left(-(\theta_s^{(p)}-\theta_{s'}^{(p)})^2\right)\right]\times$$

$$\left[\prod_{\substack{p=2 \\ k\neq k'}}^{4}\prod_{(s,s')}\beta_t^{(p)}\sqrt{t_k-t_{k'}}\exp\left(-(\theta_s^{(p)}-\theta_{s'}^{(p)})^2\right)\right]$$

$$\left[\prod_{p=2}^{4}\prod_{s}\mathbb{1}_{\Theta^{(p)}}(\theta_s^{(p)})\right]$$

$$\left[\prod_{\substack{(k,k') \\ k\neq k'}}\beta_t^{(p)}\sqrt{t_k-t_{k'}}\exp\left(-(\theta_k^{(p)}-\theta_{k'}^{(p)})^2\right)\right]$$

$$\mathbb{1}_{\Theta^{(1)}}(\theta_k^{(1)})\times P(\sigma_{\varepsilon,k}^2) \tag{27}$$

where $\{\beta_T^{(p)}\}_{p=1,..,4}$ are the parameters of temporal regularization of the four unknown parameters.

The Gibbs sampler is then used to calculate the *a posteriori* probability

$$P(\theta_s^{(p)}|\theta_{s'\neq s}^{(p)},\theta_{s\in\Omega}^{(q\neq p)},\sigma_{\varepsilon,k}^2,R,\psi)=$$

$$\frac{P(\phi|R,\psi)}{\sum_{x\in\Theta^{(p)}}P(\phi^{(x,p)}|R,\psi)} \tag{28}$$

where

$$\phi^{(x,p)}(i)=\begin{cases}\phi(i),\ i\neq p\\ x,\quad i=p\end{cases}. \tag{29}$$

Thus, $\forall p\in\{2,\ldots,4\}$, the probability of the θ_s^p parameter knowing its neighbor is as follows:

$$P(\theta_s^{(p)}|\theta_{s'\neq s}^{(p)},\theta_{s\in\Omega}^{(q\neq p)},\sigma_{\varepsilon,k}^2,R,\psi)=$$

$$\frac{P(R_s|\phi,\psi)\prod_{\substack{(s,s') \\ k=k'}}\beta_s^{(p)}\exp\left(-\left(\theta_s^{(p)}-\theta_{s'}^{(p)}\right)^2\right)}{\sum_{x\in\Theta^{(p)}}P(R_s|x,\psi)\prod_{(s,s')}\exp\left(-\left(x-\theta_{s'}^{(p)}\right)^2\right)}\times$$

$$\prod_{\substack{(s,s') \\ k\neq k'}}\beta_t^{(p)}\sqrt{t_k-t_{k'}}\exp\left(-(\theta_s^{(p)}-\theta_{s'}^{(p)})^2\right)=$$

$$\frac{\prod_{(s,s')\in C}\exp\left[-\left(\theta_s^{(p)}-\theta_{s'}^{(p)}\right)^2\right]P(R_s|\theta_s^{(p)},\theta_s^{(q\neq p)},\theta_s^{(1)},\sigma_{\varepsilon,k}^2,\psi)}{\sum_{x\in\Theta^{(p)}}\prod_{(s,s')\in C}\exp\left[-\left(x-\theta_{s'}^{(p)}\right)^2\right]P(R_s|x,\theta_s^{(q\neq p)},\theta_s^{(1)},\sigma_{\varepsilon,k}^2,\psi)}=$$

$$\frac{\exp-\left(\sum_{(s,s')\in C}(\theta_s^{(p)}-\theta_{s'}^{(p)})^2\right)P(R_s|\theta_s^{(p)},\theta_s^{(q\neq p)},\theta_s^{(1)},\sigma_{\varepsilon,k}^2,\psi)}{\sum_{x\in\Theta^{(p)}}\exp-\left(\sum_{(s,s')\in C}(x-\theta_{s'}^{(p)})^2\right)P(R_s|x,\theta_s^{(q\neq p)},\theta_s^{(1)},\sigma_{\varepsilon,k}^2,\psi)}=$$

$$\frac{\exp\left(-\sum_{(s,s')\in C}(\theta_s^{(p)}-\theta_{s'}^{(p)})^2-\frac{\|f(\theta_s)-R_s\|^2}{2\sigma_{\varepsilon,k}^2}\right)}{\sum_{x\in\Theta^{(p)}}\exp\left(-\sum_{(s,s')\in C}(x-\theta_{s'}^{(p)})^2-\frac{\|f(\theta_s^{(x,p)})-R_s\|^2}{2\sigma_{\varepsilon,k}^2}\right)} \tag{30}$$

where

$$\theta_s^{(x,p)}(i)=\begin{cases}\theta_s(i)\ \forall i\neq p\\ x,\quad i=p\end{cases}. \tag{31}$$

For $p=1$, the probability of θ_k^1 taking into account only temporal variation is as follows:

$$P(\theta_k^{(1)}|\theta_{k\neq k'}^{(1)},\sigma_{\varepsilon,k}^2,R,\psi)=$$

$$\frac{P(R_s|\phi,\psi)\prod_{(k,k')\in C_K}\beta_t^{(1)}\sqrt{t_k-t_{k'}}\exp\left(-(\theta_k^{(1)}-\theta_{k'}^{(1)})^2\right)}{\sum_{x\in\Theta^{(p)}}P(R_s|x,\psi)\prod_{(k,k')\in C_K}\exp\left(-(x-\theta_{k'}^{(p)})^2\right)}=$$

$$\frac{\prod_{(k,k')\in C_K}\exp-\left(\theta_k^{(1)}-\theta_{k'}^{(1)}\right)^2P(R_s|\theta_s^{(p)},\sigma_{\varepsilon,k}^2,\psi)}{\sum_{x\in\Theta^{(p)}}\prod_{(k,k')\in C_K}\exp-\left(x-\theta_{k'}^{(p)}\right)^2P(R_s|x,\sigma_{\varepsilon,k}^2,\psi)}=$$

$$\frac{\exp-\left(\sum_{(k,k')\in C_K}(\theta_k^{(1)}-\theta_{k'}^{(1)})^2\right)P(R_s|\theta_s^{(p)},\sigma_{\varepsilon,k}^2,\psi)}{\sum_{x\in\Theta^{(p)}}\exp-\left(\sum_{(k,k')\in C_K}(x-\theta_{k'}^{(p)})^2\right)P(R_s|x,\sigma_{\varepsilon,k}^2,\psi)}=$$

$$\frac{\exp\left(-\sum_{(k,k')\in C_K}(\theta_k^{(1)}-\theta_{k'}^{(1)})^2-\frac{\|f(\theta_s)-R_s\|^2}{2\sigma_{\varepsilon,k}^2}\right)}{\sum_{x\in\Theta^{(p)}}\exp\left(-\sum_{(k,k')\in C_K}(x-\theta_{k'}^{(p)})^2-\frac{\|f(\theta_s^{(x,1)})-R_s\|^2}{2\sigma_{\varepsilon,k}^2}\right)}. \tag{32}$$

Also, $\sigma_{\varepsilon,k}^2$ is estimated as

$$P(\sigma_{\varepsilon,k}^2|\phi\setminus\{\sigma_{\varepsilon,k}^2\},R,\psi)\propto$$

$$P(R|\sigma_{\varepsilon,k}^2,\phi\setminus\{\sigma_{\varepsilon,k}^2\},\psi)P(\sigma_{\varepsilon,k}^2)\propto$$

$$\prod_{s}P(R_s|\sigma_{\varepsilon,k}^2,\phi\setminus\{\sigma_{\varepsilon,k}^2\},\psi)P(\sigma_{\varepsilon,k}^2)\propto$$

$$\frac{1}{\sqrt{2\Pi\sigma_{\varepsilon,k}^2}}^{\frac{(N_bN_rN_c)}{2}}\exp\left(-\frac{\sum_s\|f(\theta_s)-R_s\|^2}{2\sigma_{\varepsilon,k}^2}\right)$$

$$P(\sigma_{\varepsilon,k}^2)\propto$$

$$IG\left(\alpha+\frac{N_bN_rN_c}{2},\frac{\sum_s\|f(\theta_s)-R_s\|^2}{2}+\beta\right). \tag{33}$$

REFERENCES

[1] D. Haboudane, J. R. Miller, E. Pattey, P. J. Zarco-Tejada, and I. B. Strachan, "Hyperspectral vegetation indices and novel algorithms for predicting green LAI of crop canopies: Modeling and validation in the context of precision agriculture," *Remote Sens. Environ.*, vol. 90, no. 3, pp. 337–352, 2004.

[2] C. D. Allen *et al.*, "A global overview of drought and heat-induced tree mortality reveals emerging climate change risks for forests," *Forest Ecol. Manage.*, vol. 259, no. 4, pp. 660–684, 2010.

[3] P. J. Zarco-Tejada, A. Hornero, P. Beck, T. Kattenborn, P. Kempeneers, and R. Hernández-Clemente, "Chlorophyll content estimation in an open-canopy conifer forest with Sentinel-2a and hyperspectral imagery in the context of forest decline," *Remote Sens. Environ.*, vol. 223, pp. 320–335, 2019.

[4] S. Manna and B. Raychaudhuri, "Retrieval of leaf area index and stress conditions for Sundarban mangroves using Sentinel-2 data," *Int. J. Remote Sens.*, vol. 41, no. 3, pp. 1019–1039, 2020.

[5] R. Darvishzadeh *et al.*, "Analysis of Sentinel-2 and RapidEye for retrieval of leaf area index in a saltmarsh using a radiative transfer model," *Remote Sens.*, vol. 11, no. 6, 2019, Art. no. 671.

[6] M. Lange, B. Dechant, C. Rebmann, M. Vohland, M. Cuntz, and D. Doktor, "Validating modis and Sentinel-2 NDVI products at a temperate deciduous forest site using two independent ground-based sensors," *Sensors*, vol. 17, no. 8, 2017, Art. no. 1855.

[7] G. S. Sibbett and L. Ferguson, *Olive Production Manual*, vol. 3353. Davis, CA, USA: UCANR Publications, 2005.

[8] R. Houborg and M. F. McCabe, "High-resolution NDVI from planet's constellation of Earth observing nano-satellites: A new data source for precision agriculture," *Remote Sens.*, vol. 8, no. 9, 2016, Art. no. 768.

[9] R. Houborg and M. F. McCabe, "A cubesat enabled spatio-temporal enhancement method (CESTEM) utilizing planet, landsat and MODIS data," *Remote Sens. Environ.*, vol. 209, pp. 211–226, 2018.

[10] O. Csillik, P. Kumar, J. Mascaro, T. O'Shea, and G. P. Asner, "Monitoring tropical forest carbon stocks and emissions using planet satellite data," *Sci. Rep.*, vol. 9, no. 1, pp. 1–12, 2019.

[11] S. L. Ustin *et al.*, "Retrieval of foliar information about plant pigment systems from high resolution spectroscopy," *Remote Sens. Environ.*, vol. 113, pp. S67–S77, 2009.

[12] N. S. Goel, "Models of vegetation canopy reflectance and their use in estimation of biophysical parameters from reflectance data," *Remote Sens. Rev.*, vol. 4, no. 1, pp. 1–212, 1988.

[13] S. Chaabouni, A. Kallel, and R. Houborg, "Improving retrieval of crop biophysical properties in dryland areas using a multi-scale variational RTM inversion approach," *Int. J. Appl. Earth Observ. Geoinf.*, vol. 94, 2021, Art. no. 102220.

[14] C. Atzberger and K. Richter, "Spatially constrained inversion of radiative transfer models for improved LAI mapping from future Sentinel-2 imagery," *Remote Sens. Environ.*, vol. 120, pp. 208–218, 2012.

[15] I. Bye *et al.*, "Estimating forest canopy parameters from satellite waveform LiDAR by inversion of the FLIGHT three-dimensional radiative transfer model," *Remote Sens. Environ.*, vol. 188, pp. 177–189, 2017.

[16] R. Hernández-Clemente, P. R. North, A. Hornero, and P. J. Zarco-Tejada, "Assessing the effects of forest health on sun-induced chlorophyll fluorescence using the fluorflight 3-D radiative transfer model to account for forest structure," *Remote Sens. Environ.*, vol. 193, pp. 165–179, 2017.

[17] T. J. Assal, P. J. Anderson, and J. Sibold, "Spatial and temporal trends of drought effects in a heterogeneous semi-arid forest ecosystem," *Forest Ecol. Manage.*, vol. 365, pp. 137–151, 2016.

[18] J. Gastellu-Etchegorry, E. Martin, and F. Gascon, "DART: A 3D model for simulating satellite images and studying surface radiation budget," *Int. J. Remote Sens.*, vol. 25, no. 1, pp. 73–96, 2004.

[19] F. Gascon, J.-P. Gastellu-Etchegorry, M.-J. Lefevre-Fonollosa, and E. Dufrene, "Retrieval of forest biophysical variables by inverting a 3-D radiative transfer model and using high and very high resolution imagery," *Int. J. Remote Sens.*, vol. 25, no. 24, pp. 5601–5616, 2004.

[20] R. Zurita-Milla, V. Laurent, and J. van Gijsel, "Visualizing the ill-posedness of the inversion of a canopy radiative transfer model: A case study for Sentinel-2," *Int. J. Appl. Earth Observ. Geoinf.*, vol. 43, pp. 7–18, 2015.

[21] B. Combal *et al.*, "Retrieval of canopy biophysical variables from bidirectional reflectance: Using prior information to solve the ill-posed inverse problem," *Remote Sens. Environ.*, vol. 84, no. 1, pp. 1–15, 2003.

[22] C. Bacour, F. Baret, D. Béal, M. Weiss, and K. Pavageau, "Neural network estimation of LAI, fAPAR, fCover and LAI × Cab, from top of canopy MERIS reflectance data: Principles and validation," *Remote Sens. Environ.*, vol. 105, no. 4, pp. 313–325, 2006.

[23] R. Darvishzadeh *et al.*, "Mapping leaf chlorophyll content from Sentinel-2 and RapidEye data in spruce stands using the invertible forest reflectance model," *Int. J. Appl. Earth Observ. Geoinf.*, vol. 79, pp. 58–70, 2019.

[24] P. Varvia, M. Rautiainen, and A. Seppänen, "Modeling uncertainties in estimation of canopy LAI from hyperspectral remote sensing data— A Bayesian approach," *J. Quantitative Spectrosc. Radiative Transfer*, vol. 191, pp. 19–29, 2017.

[25] V. C. Laurent, M. E. Schaepman, W. Verhoef, J. Weyermann, and R. O. Chávez, "Bayesian object-based estimation of LAI and chlorophyll from a simulated Sentinel-2 top-of-atmosphere radiance image," *Remote Sens. Environ.*, vol. 140, pp. 318–329, 2014.

[26] A. N. Shiklomanov, M. C. Dietze, T. Viskari, P. A. Townsend, and S. P. Serbin, "Quantifying the influences of spectral resolution on uncertainty in leaf trait estimates through a Bayesian approach to RTM inversion," *Remote Sens. Environ.*, vol. 183, pp. 226–238, 2016.

[27] Q. Zhang, X. Xiao, B. Braswell, E. Linder, F. Baret, and B. Moore III, "Estimating light absorption by chlorophyll, leaf and canopy in a deciduous broadleaf forest using MODIS data and a radiative transfer model," *Remote Sens. Environ.*, vol. 99, no. 3, pp. 357–371, 2005.

[28] S. Junttila *et al.*, "Measuring leaf water content with dual-wavelength intensity data from terrestrial laser scanners," *Remote Sens.*, vol. 9, no. 1, 2017, Art. no. 8.

[29] H. K. Lichtenthaler, "Chlorophylls and carotenoids: Pigments of photosynthetic biomembranes," *Methods Enzymol.*, vol. 148, pp. 350–382, 1987.

[30] G. Caruso *et al.*, "High-resolution imagery acquired from an unmanned platform to estimate biophysical and geometrical parameters of olive trees under different irrigation regimes," *PLoS One*, vol. 14, no. 1, 2019, Art. no. e0210804.

[31] S. Jacquemoud and F. Baret, "PROSPECT: A model of leaf optical properties spectra," *Remote Sens. Environ.*, vol. 34, no. 2, pp. 75–91, 1990.

[32] N. Agam, W. P. Kustas, M. C. Anderson, F. Li, and P. D. Colaizzi, "Utility of thermal sharpening over Texas high plains irrigated agricultural fields," *J. Geophys. Res.: Atmos.*, vol. 112, no. D19, p. 10, 2007.

[33] M. R. Gupta and Y. Chen, "Theory and use of the EM algorithm," *Found. Trends Signal Process.*, vol. 4, no. 3, pp. 223–296, 2011.

[34] V. Patel and K. Mistree, "A review on different image interpolation techniques for image enhancement," *Int. J. Emerg. Technol. Adv. Eng.*, vol. 3, no. 12, pp. 129–133, 2013.

[35] P. Bowyer, F. Danson, and N. Trodd, "Methods of sensitivity analysis in remote sensing: Implications for canopy reflectance model inversion," in *Proc. IEEE Int. Geosci. Remote Sens. Symp.*, 2003, vol. 6, pp. 3839–3841.

[36] Q. Xie *et al.*, "Retrieval of crop biophysical parameters from Sentinel-2 remote sensing imagery," *Int. J. Appl. Earth Observ. Geoinf.*, vol. 80, pp. 187–195, 2019.

[37] M. A. Mezghani, G. Hassouna, L. Ibtissem, and F. Labidi, "Leaf area index and light distribution in olive tree canopies," *Int. J. Agronomy Agricultural Res.*, vol. 8, no. 5, pp. 60–65, May 2016.

[38] L. Suárez, P. Zarco-Tejada, J. Berni, V. González-Dugo, and E. Fereres, "Modelling PRI for water stress detection using radiative transfer models," *Remote Sens. Environ.*, vol. 113, no. 4, pp. 730–744, 2009.

[39] J. Verrelst *et al.*, "Optical remote sensing and the retrieval of terrestrial vegetation bio-geophysical properties—A review," *ISPRS J. Photogrammetry Remote Sens.*, vol. 108, pp. 273–290, 2015.

[40] A. Banskota *et al.*, "An LUT-based inversion of DART model to estimate forest LAI from hyperspectral data," *IEEE J. Sel. Topics Appl. Earth Observ. Remote Sens.*, vol. 8, no. 6, pp. 3147–3160, Jun. 2015.

[41] T. Miraglio, K. Adeline, M. Huesca, S. Ustin, and X. Briottet, "Monitoring LAI, chlorophylls, and carotenoids content of a woodland savanna using hyperspectral imagery and 3D radiative transfer modeling," *Remote Sens.*, vol. 12, no. 1, 2020, Art. no. 28.

[42] R. Houborg, M. Anderson, and C. Daughtry, "Utility of an image-based canopy reflectance modeling tool for remote estimation of LAI and leaf chlorophyll content at the field scale," *Remote Sens. Environ.*, vol. 113, no. 1, pp. 259–274, 2009.

[43] J. Jiang, Z. Xiao, J. Wang, and J. Song, "Sequential method with incremental analysis update to retrieve leaf area index from time series MODIS reflectance data," *Remote Sens.*, vol. 6, no. 10, pp. 9194–9212, 2014.

[44] M. Monsi and T. Saeki, "On the factor light in plant communities and its importance for matter production," *Ann. Botany*, vol. 95, no. 3, pp. 549–567, 2005.

[45] X. Yang, C. Wang, F. Pan, S. Nie, X. Xi, and S. Luo, "Retrieving leaf area index in discontinuous forest using ICESAT/GLAS full-waveform data based on gap fraction model," *ISPRS J. Photogrammetry Remote Sens.*, vol. 148, pp. 54–62, 2019.

[46] M. Mariscal, F. Orgaz, and F. Villalobos, "Modelling and measurement of radiation interception by olive canopies," *Agricultural Forest Meteorol.*, vol. 100, no. 2/3, pp. 183–197, 2000.

[47] B. Zhao, Y. Zhong, A. Ma, and L. Zhang, "A spatial Gaussian mixture model for optical remote sensing image clustering," *IEEE J. Sel. Topics Appl. Earth Observ. Remote Sens.*, vol. 9, no. 12, pp. 5748–5759, Dec. 2016.

[48] W. Verhoef, "Light scattering by leaf layers with application to canopy reflectance modeling: The sail model," *Remote Sens. Environ.*, vol. 16, no. 2, pp. 125–141, 1984.

[49] A. Kallel and T. Nilson, "Revisiting the vegetation hot spot modeling: Case of Poisson/binomial leaf distributions," *Remote Sens. Environ.*, vol. 130, pp. 188–204, 2013.

[50] J. Gómez, P. Zarco-Tejada, J. García-Morillo, J. Gama, and M. Soriano, "Determining biophysical parameters for olive trees using CASI-airborne and quickbird-satellite imagery," *Agronomy J.*, vol. 103, no. 3, pp. 644–654, 2011.

[51] A. Damm *et al.*, "Data acquisition report 2011," *Remote Sens. Laboratories*, Zurich, Switzerland, 2010.

[52] A. Damm *et al.*, "Remote sensing of sun-induced fluorescence to improve modeling of diurnal courses of gross primary production (GPP)," *Global Change Biol.*, vol. 16, no. 1, pp. 171–186, 2010.

[53] V. C. Laurent, W. Verhoef, A. Damm, M. E. Schaepman, and J. G. Clevers, "A Bayesian object-based approach for estimating vegetation biophysical and biochemical variables from APEX at-sensor radiance data," *Remote Sens. Environ.*, vol. 139, pp. 6–17, 2013.

[54] P. J. Zarco-Tejada, J. R. Miller, A. Morales, A. Berjón, and J. Agüera, "Hyperspectral indices and model simulation for chlorophyll estimation in open-canopy tree crops," *Remote Sens. Environ.*, vol. 90, no. 4, pp. 463–476, 2004.

[55] F. Gascon *et al.*, "Copernicus Sentinel-2A calibration and products validation status," *Remote Sens.*, vol. 9, no. 6, 2017, Art. no. 584.

[56] S. Garrigues *et al.*, "Validation and intercomparison of global leaf area index products derived from remote sensing data," *J. Geophys. Res., Biogeosci.*, vol. 113, no. G2, 2008, Art. no. G02028.

[57] S. Liang, *Quantitative Remote Sensing of Land Surfaces*, vol. 30. Hoboken, NJ, USA: Wiley, 2005.

[58] R. Gucci and C. Cantini, *Pruning and Training Systems for Modern Olive Growing*. Canberra, ACT, Australia: CSIRO Publishing, 2000.

[59] F. Sanz-Cortés *et al.*, "Phenological growth stages of olive trees (Olea Europaea)," *Ann. Appl. Biol.*, vol. 140, no. 2, pp. 151–157, 2002.

[60] M. Guerfel, O. Baccouri, D. Boujnah, W. Chaïbi, and M. Zarrouk, "Impacts of water stress on gas exchange, water relations, chlorophyll content and leaf structure in the two main Tunisian olive (Olea Europaea l) cultivars," *Sci. Horticulturae*, vol. 119, no. 3, pp. 257–263, 2009.

[61] S. Lavee, "Biologie et physiologie de l'olivier," in *Encyclopédie Mondiale de l'olivier*. Barcelona, Spain: Servers Editorials Estudi Balm, 1997.

[62] Tutiempo, Accessed: Jan. 2021, [Online]. Available: https://fr.tutiempo.net/sfax.html

[63] L. A. Brown, J. Dash, A. L. Lidón, E. Lopez-Baeza, and S. Dransfeld, "Synergetic exploitation of the Sentinel-2 missions for validating the Sentinel-3 ocean and land color instrument terrestrial chlorophyll index over a vineyard dominated Mediterranean environment," *IEEE J. Sel. Topics Appl. Earth Observ. Remote Sens.*, vol. 12, no. 7, pp. 2244–2251, Jul. 2019.

Hana Abdelmoula received the Engineering degree in networks and telecommunication from the National School of Electronics and Telecommunications of Sfax, University of Sfax, Sfax, Tunisia, in 2015. She is currently working toward the Ph.D. degree in computer systems engineering and remote sensing with the University of Sfax.

She is a Student Researcher with the Digital Research Centre of Sfax, Sfax. Her research interests include satellite remote sensing, vegetation monitoring, inverse models, and algorithms for estimating vegetation properties.

Abdelaziz Kallel received the Engineering and M.S. degrees in telecommunications from the Higher School of Communication of Tunis, Aryanah, Tunisia, in 2003 and 2004, respectively, the Ph.D. degree in physics from Paris-Sud University, Orsay, France, in 2007, and the HDR degree in remote sensing image physical and statistical modeling and processing from the University of Sfax, Sfax, Tunisia, in 2014.

He was a Postdoctoral Scientist with the Laboratory of Climate and Environmental Sciences, Saint-Aubin, France, and Tartu Observatory, Tõravere, Estonia, in 2008 and 2009, respectively. He is currently a Senior Researcher of Remote Sensing with the Digital Research Centre of Sfax, Sakiet Ezzit, Tunisia. Particularly, he is the Head of the Remote Sensing for Smart Agriculture Team as well as the Laboratory of Signals, Systems, Artificial Intelligence and Networks. His research interests include radiative transfer theory and application to vegetation cover property inversion using passive and active optical remote sensing techniques.

Jean-Louis Roujean received the Ph.D. degree in geosciences and remote sensing from University Paul Sabatier, Toulouse, France, in 1991.

He was a Postdoctoral Fellow with the Centre National de Recherches Mtorologiques until he joined Centre National de Recherche Scientifique (CNRS), Paris, France, in 1994. From 1999 to 2008, he was the Head of Remote Sensing Group for Land Surface Studies. He is currently the Director of research with the CNRS. His published papers concern merely land cover classification, radiation transfer modeling for vegetation and snow, inverse modeling, data fusion and assimilation, radiative flux mapping, and validation operations. He has been involved in several framework programs of the European Union (FP5/CYCLOPES, FP6/GEOLAND, and FP7/ImagineS), and more recently the Global Land Service of Copernicus. For almost 20 years, he was responsible for the development and operational implementation of shortwave radiative fluxes products for Meteosat and Metop spacebornes in the frame of the Consortium Land Surface Analysis for Satellite Application Facilities on under an EUMETSAT contract. He also participated in international field experiments like HAPEX-Sahel (1992), BOREAS (1994), and SNORTEX (2008–2010) for measuring radiative transfer at various scales. His research interests include the modeling of the surface bidirectional reflectance distribution function and albedo.

Dr. Roujean is the Principal Investigator for France of the Thermal Infrared TRISHNA Mission.

Jean-Philippe Gastellu-Etchegorry received the Ph.D. degree in solar physics and the Ph.D. degree in remote sensing and digital image processing from Paul Sabatier University (PSU), Toulouse, France, in 1983 and 1989, respectively.

In 1990, after five years with Gadjah Mada University Remote Sensing Center (Indonesia) and Bangkok (Thailand), he was an Associate Professor with PSU and led the IRAP Remote Sensing team. In 1995, he joined the Centre d'Etudes Spatiales de la Biosphère (CESBIO), where he led the modeling team for 15 years. In 1997, he was a Full Professor with PSU. For 17 years, he headed the AUF Remote Sensing Society (3000 members). Since 2007, he has been a CESBIO Deputy Director and President of the Scientific Council of IUT, a Major Faculty with PSU. Since 1992, he has been the Head of the team that develops the discrete anisotropic radiative transfer (DART) model that simulates fluorescence, radiative budget, and satellite/airborne/in-situ spectroradiometer and LiDAR acquisitions of natural and urban landscapes. DART was patented in 2003. PSU gave 460 licenses to research and space centers (NASA, KCL, CAS, etc.). He has authored or coauthored 168 papers (rate A), three books, and book chapters. His research interests include radiative transfer modeling and applications.

Prof. Gastellu-Etchegorry is a Co-Chair of the Modeling in Remote Sensing Technical Committee of the IEEE Geoscience and Remote Sensing Society and the Executive Editor for *Journal of Remote Sensing*.